8.3.3.2 Magnetic structure

At 2K a series of additional Bragg peaks are present at low angles and are clear indications of the presence of AFM ordering (T_N 125K). The low temperature magnetic peaks can be indexed using a commensurate propagation vector. In the precedent section, the analysis of the superlattice peaks revealed the existence of different structural modulations that are related to different orbital ordered. The magnetic order is strongly related to the orbital order. For that reason, the magnetic structure that we obtain in our analysis should be considered as an average description of the magnetic order existing at each orbitally ordered region. From the analysis of the superstructure peaks using SXRPD, we measured larger coherence lengths for 2a×3b×c and a×3b×c domains. Therefore, we have decided to analyse the magnetic structure based on the *a×3b×c* tripled cell. Inspection of the magnetic peaks suggests that the AFM cell consists then in a 2*a*×3*b*×*c*.

The model that better fitted our NPD data consists in a Wigner crystal type model. The magnetic structure found and the orbital order agree and are

Fig. 8-35 *AFM structure of $Bi_{1/3}Ca_{2/3}MnO_3$ as refined from NPD.*

shown in Fig. 8-35. The magnetic model is consistent with the models reported by Radaelli et al. and Fernandez Diaz et al. for lanthanum based compound.

In this model, the Mn^{+3} tend to be as far apart as possible and have their d_z^2 occupied orbital pointing towards one of the in-plane Mn^{+4} first neighbours. That can explain why upon cooling down the cell parameter perpendicular to these planes is highly reduced. The ordered moment of the Mn^{+3} ions is nearly FM coupled with its two neighbouring Mn^{+4} ions and is found to be in the *ab* plane.

The magnetic structure can be described as a kind of striped arrangement of "polarons" formed by FM aligned groups of three Mn (Mn^{+4}-Mn^{+3}-Mn^{+4}). In Fig. 8-35 the "polarons" are schematically highlighted. The moments of neighbouring polarons are coupled AFM in the *a* direction, while in *b* direction neighbouring polarons have their moments pointing almost perpendicular.

The relative orientation of neighbouring Mn^{+4} is non colinear and would tend to be AFM as expected from the SE interaction governing the Mn^{+4}-Mn^{+4} magnetic interaction. In Fig. 8-36 is shown a zoom of a selected zone of the diffraction pattern showing the AFM peaks and the fit using the
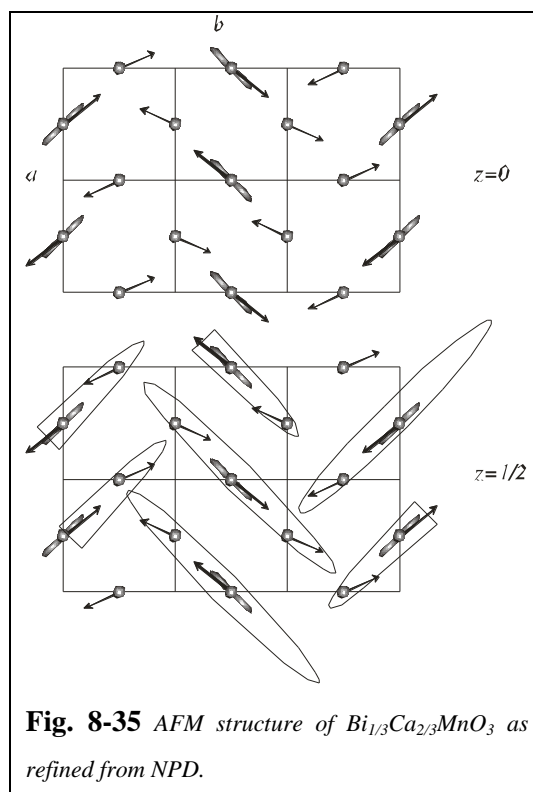
model explained above. In Fig. 8-27 is shown the whole SXRPD and NPD patterns obtained from joint refinement.

The refinement of the magnetic structure was performed using several constrains linking the magnetic atoms and their interactions because of the large number of atoms in the magnetic structure and the small number of magnetic peaks. We supposed two types of magnetic atoms that can be associated to Mn^{+3} and to Mn^{+4}. The coupling between Mn^{+3} in the x direction is supposed to be completely AFM. The reason for
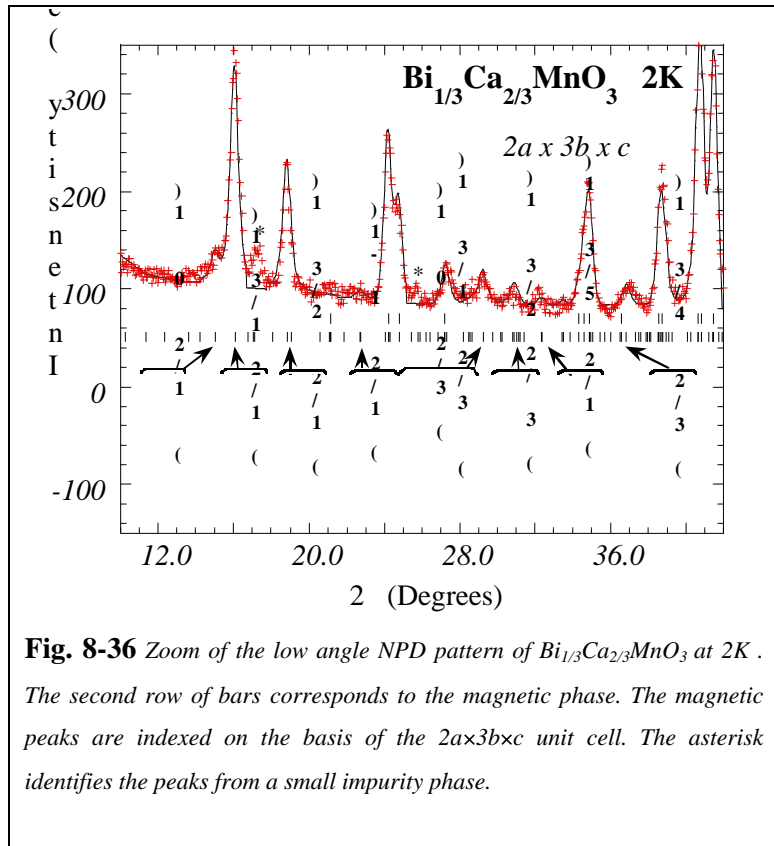

Fig. 8-36 *Zoom of the low angle NPD pattern of $Bi_{1/3}Ca_{2/3}MnO_3$ at 2K . The second row of bars corresponds to the magnetic phase. The magnetic peaks are indexed on the basis of the 2a×3b×c unit cell. The asterisk identifies the peaks from a small impurity phase.*

such assumption can be found in the fact that the magnetic cell is doubled in this direction. On the other hand, as we observed superlattice peaks with (0,1/3,0) propagation vector, that means that the orbital order of Mn^{+3} should be rotated in the direction of the tripling of the cell. If not such rotation exist, the structural cell would no be tripled.

The magnetic moments of the magnetic atom associated to Mn^{+3} ions are found to be oriented close to the direction of the d_Z^2 orbitals and thus, that determines the Mn^{+3} network which is identified by one angle   128(24)° for the Mn in the position (1/4, 0, 0). The obtained magnetic moment for the magnetic atom associated to Mn^{+3} is about 3.2(8)μ_B/Mn

The Mn^{+4} network has been built up considering the possible magnetic interactions extracted from Goodenough early works [17]. Hence, two neighbouring Mn^{+4} would tend to be AFM coupled (SE) and a Mn^{+3} –Mn^{+4} would be FM. The Mn^{+4} network has been characterised by one angle   115(11) for the Mn in position (0, 1/3, 0). The obtained moment for Mn^{+4} ion is about 2.6(5)μ_B/Mn.

In Tab. 8-IX are shown the refined moments and angles as well as the magnetic coupling between magnetic atoms. The magnetic refinement converged giving a magnetic R-factor   12.

The refinement considering equal moments converged to Mn(I)=Mn(II)= 2.72(1) μ_B/Mn but the refinement did not improve: R_{Mag}=18. Nevertheless, due to the coexistence of different orbitally ordered domains, we expect to obtain an averaged magnetic structure. In this sense a similar magnetic model could be constructed considering a $3a×2b×c$ magnetic cell as suggested by Fernandez Diaz et

al. It is hardly visible from the magnetic peaks the difference between the two models because the real magnetic structure should be a mixture of both taking into account the strong relationship between the magnetic order and the orbital order and the fact that superlattice peaks of both structural modulations are observed by SXRPD.

Tab. 8-X. Results of the magnetic refinement of the NPD data on $Bi_{1/3}Ca_{2/3}MnO_3$

	Site		m (μ_B/Mn)	Phi
	(1/4,0,0)	(1/4,0,0)	3.2(8) ×	128(24)
		(3/4,0,0)	-1	
		(1/4,0,1/2)	-1	
		(3/4,0,1/2)	+1	
	(0,1/2,0)	(0,1/2,0)	3.2(8)×	51(24)
Mn^{+3}=3.2 (8)		(1/2,1/2,0)	-1	
		(0,1/2,1/2)	-1	
		(1/2,1/2,1/2)	+1	
	(1/4,2/3,0)	(1/4,2/3,0)	2.6(5)	295(11)
		(3/4,2/3,0)	-1	
		(1/4,2/3,1/2)	-1	
		(3/4,2/3,1/2)	+1	
	(0,5/6,0)	(0,5/6,0)	2.6(5)	295(11)
		(1/2,5/6,0)	-1	
		(0,5/6,1/2)	-1	
		(1/2,5/6,1/2)	+1	
	(0,1/6,0)	(0,1/6,0)	2.6(5)	115(11)
		(1/2,1/6,0)	-1	
		(0,1/6,1/2)	-1	
Mn^{+4}=2.6(5)		(1/2,1/6,1/2)	+1	
	(1/4,1/3,0)	(1/4,1/3,0)	2.6(5)	-115(11)
		(3/4,1/3,0)	-1	
		(1/4,1/3,1/2)	-1	
		(3/4,1/2,1/2)	+1	

8.3.4 Conclusions

We have performed an extensive characterisation of $Bi_{1/3}Ca_{2/3}MnO_3$ compound. From magnetisation and resistivity measurements, we concluded that below T_{CO} 300K the compound develops an orbital order and that below T_N=125K it is magnetically ordered. The T_{CO} obtained in $Bi_{1/3}Ca_{2/3}MnO_3$ is about 30K above the reported charge ordering temperature in the lanthanum parent compound (T_{C0}=270K) while the magnetic ordering in bismuth based compound, takes place at about 40K below the magnetic ordering temperature in the lanthanum based compound.

$Bi_{1/3}Ca_{2/3}MnO_3$ compound has been found to be single phase at high temperature with only small impurity (1.3% in volume). The analysis of the averaged unit cell allowed to monitor the anisotropic evolution of the cell parameters at T_{CO}, which is a clear signature of a particular orbital ordering where the d_z^2 full orbitals are polarised in the *ab* plane. This particular orbital ordering produces an expansion of the in-plane cell parameters and a decrease of the distance between the planes where the orbitals are polarised.

The comparison of the Mn-O bond distances and angles in $Bi_{1/3}Ca_{2/3}MnO_3$ and $La_{1/3}Ca_{2/3}MnO_3$ shows that bismuth based compound is more distorted than lanthanum compound. In addition, the oxygen octahedra have been found to be highly anisotropic in bismuth compound. In fact, the oxygen octahedra was found to be unusually expanded in the equatorial *ab* plane below T_{CO} and highly compressed in the apical direction. In addition, an expansion of the mean <Mn-O> distance compared to the lanthanum based compound has been reported. The anisotropic distortion of the oxygen octahedra as well as the expansion of the <Mn-O> distance do not favour the DE interaction and thus, they contribute to the localisation of the carriers.

Structural modulations are detected below T_{CO}. The inspection of the superlattice peaks characterising the structural modulations suggests that the ground state is quasi-degenerate. There coexist perpendicular structural modulations with a tripling of one of the in-plane (*a* or *b*) cell parameters and larger cells. A detailed study of the superlattice reflections appearing at 10K in SXPD and NPD patterns has been performed. Thanks to the different *a* and *b* cell parameters at low temperature and to the high resolution of the SXRPD data obtained at BM16 (ESRF), it has been possible to find in this compound the coexistence of different structural modulation vectors which have their origin in the stabilisation of different orbital orderings. We have identified the coexistence of large domains (2000Å) with a $q_4 = (1/2\ 1/3\ 0)$ propagation vector coexisting with domains with structural modulation $q_2 = (0\ 1/3\ 0)$ of about 800Å. In addition, smaller domains with perpendicular modulation vector were also found with dimensions of few hundreds of angstrom with $q_1 = (1/3\ 0\ 0)$ and $q_3 = (1/3\ 1/2\ 0)$ propagation vectors

The averaged magnetic structure has been determined from D2B NPD data. It has been shown to be very similar to the structure found by [210] and [209] consisting in a Wigner crystal type ordering. In the magnetic structure, the orbital order is coupled to the magnetic order. The magnetic arrangement shows the existence of FM units formed by groups $Mn^{+4}-Mn^{+3}-Mn^{+4}$ along the d_z^2 direction. The DE interaction could be at the origin of the FM alignment of the Mn ions within these units. In such case we would expect to have indistinguishable magnetic moments in Mn(I) and Mn(II) sites, which can not be ruled out from our data because of the coexistence of different orbital ordered domains at low temperatures

Our study reveals the existence of a quasi-degenerated ground state where several orbital ordered configurations are close in energy. The stabilisation of a certain orbital order determines the structural modulations and magnetic interactions. For that reason, taking into account that high-resolution SXRPD studies revealed the existence of different kinds of structural modulations, any structural or magnetic description is an oversimplification. In this sense, SXRPD studies are essential to understand the complex nature of the orbital order and charge order in these compounds.

_____

8.4 Phase segregation and magnetoresistance in $Bi_{1-x}Ca_xMnO_3$ (x>0.75)

In this section we present the study on two compounds of the $Bi_{1-x}Ca_xMnO_3$ family highly hole doped. The compounds studied are the x=0.85 and x=0.875 and correspond to concentrations were magnetoresistance (MR) has been observed. The aim of this section is to understand the origin of the MR and macroscopic phase segregation in these compounds from a macroscopic study using high resolution SXRPD and NPD data.

8.4.1 Introduction

It has been reported experimentally the existence of two regions in the manganite phase diagram where MR appears. The first region is found over a rather wide composition range (around x 30%) in the lightly hole doped regime and the second was unexpectedly found in a narrow composition range in the heavily hole doped region of Ca doped manganites [5]. In compounds with larger bandwidth like $Pr_{0.15}Sr_{0.85}MnO_3$ no MR has been evidenced [217].

The relationship between magnetoresistance and phase separation in the heavily doped and lightly doped compounds makes nanoscopic and macroscopic phase segregation a current hot topic that deserves much attention [151, 206, 234].

In manganese oxides, electronic phase separation has been theoretically proposed to occur in both the lightly (0.1<x<0.2) and heavily doped regions (0.75-0.95) of the phase diagram [159]. Phase coexistence phenomena has been observed in most of the heavily hole doped samples in manganite compounds in the region where MR is observed [5]. Similarly, in certain compounds exhibiting CMR, like $La_{0.25}Pr_{0.35}Ca_{0.375}MnO_3$, [41, 206] phase separation into a CO and a metallic phase has been suggested and observed at the metal insulator transition temperatures.

For that reasons we have performed a detailed study in the heavily doped (x>0.75) region of the $Bi_{1-x}Ca_xMnO_3$ family of compounds. Polycrystalline ceramics with compositions x=0.85 and x=0.875 exhibit MR, a non saturated FM state at low temperatures, and they are in the border line where FM in the highly doped region disappears as inferred from the early studies [224] and [227]. Moreover, if the lone pair character in Bi^{+3} is not dominant, as we have deduced in lower doping compounds, Bi^{+3} ion should acquire an effective radius between Pr and Sm, and the FM border line in this case is expected about 0.86<x<0.875.

8.4.2 Resistivity and magnetic characterisation

Resistivity measurements were performed at zero applied magnetic field upon cooling and warming (1.5K to 350K) on well characterised ceramic bars of the Bi$_{1-x}$Ca$_x$MnO$_3$ in the doping range 0.5 x 0.875 (Fig. 8-37).

The compounds with Ca content 0.5 x 0.75 exhibit an insulating behaviour in the whole range of temperatures, and there is no evidence of thermally induced insulator to metal transition upon cooling. In addition, the compounds exhibiting CO (x=1/2, x=2/3) display large values of the resistivity at low temperatures.

Fig. 8-37 *Resistivity measurements at zero applied magnetic field for the heavily doped Bi$_{1-x}$Ca$_x$MnO$_3$ regime*

Heavily hole doped compounds (x=0.85 and x=0.875) show smaller resistivity at RT and display a semi-metallic like behaviour down to the electrical transition temperature which rends them insulating. Moreover, the semi-metallic like behaviour has not been observed in the low doping regime. The origin of the semi-metallic behaviour has been suggested to be related to the weak Jahn Teller effect and associated distortions in the Mn^{+4} rich region [213-216].

For compounds with x 0.85 an increase of the resistivity is observed below a certain temperature, but the values of the resistivity at low temperatures are smaller than for the x=1/2 and x=2/3 compounds indicating the possible lack of charge ordering for these compositions, similarly to what was observed in Pr$_{1/2}$Sr$_{1/2}$MnO$_3$ compound discussed in chapter 6.

Similar transport behaviour has been found in the reported highly hole doped region of the Sm$_{1-x}$Ca$_x$MnO$_3$ family of compounds [235] and others [5] and in measurements performed on similar bismuth based manganite compounds ([227] and [224]).

Fig. 8-39 shows the resistivity curves for x=0.85 and x=0.875 samples under different applied fields up to 7T. Both samples exhibit magnetoresistance. However the MR does not only exist at the semi-metallic to insulating transition temperature as is the case of the La$_{2/3}$(Ca,Sr)$_{1/3}$MnO$_3$ samples exhibiting CMR. In this case, MR exists at any temperature below the semi-metallic to insulating transition temperature. The x=0.85 sample display a MR of about 97% at low temperatures in agreement with previously reported MR values for the Sm0.$_{15}$Ca$_{0.85}$MnO$_3$ compound [217] and for

_____

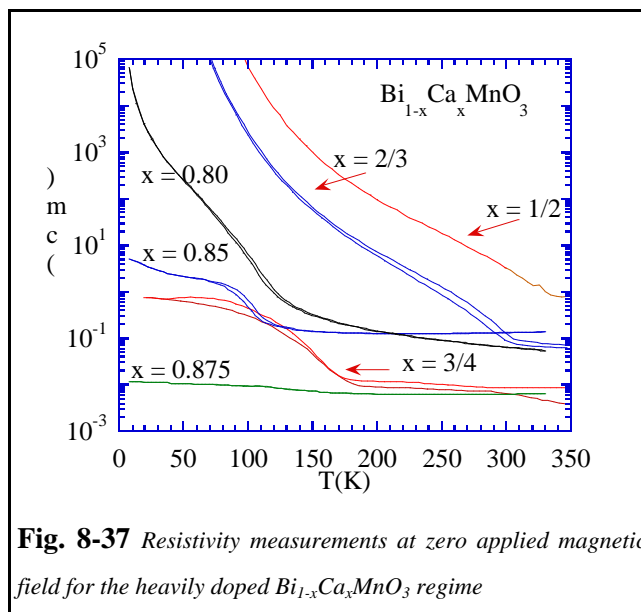$La_{0.10}Ca_{0.90}MnO_3$ [5]. In comparison, the x=0.875 compound has smaller value of the MR 52% at low temperatures (Fig. 8-39).
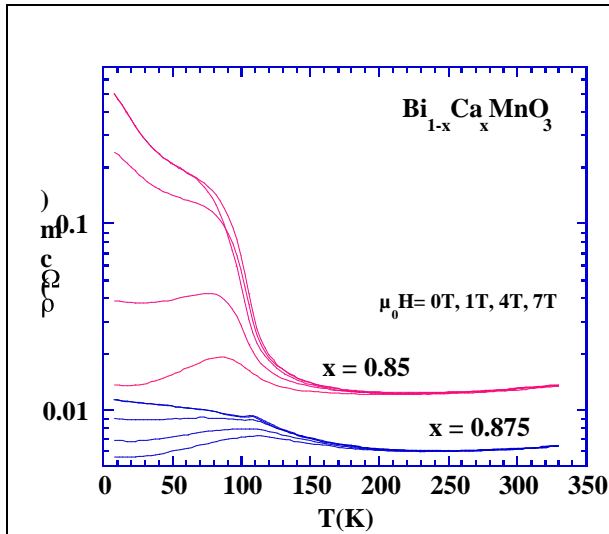

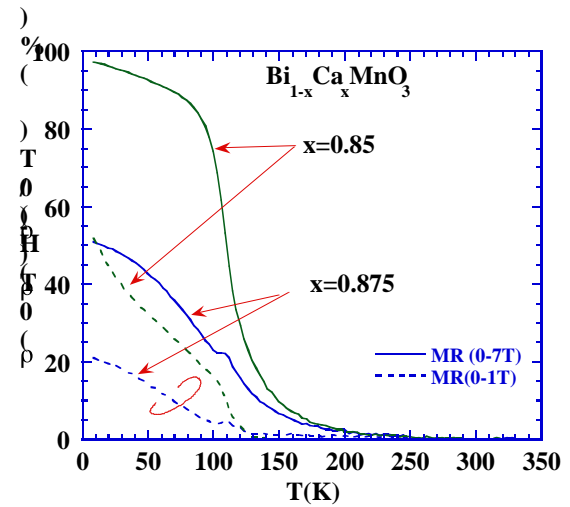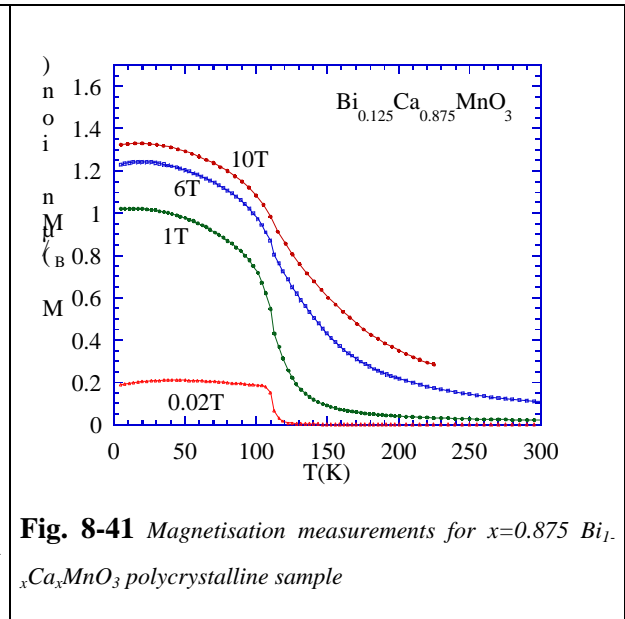**Fig. 8-38** *Thermal evolution of the resistivity under several applied magnetic fields.*
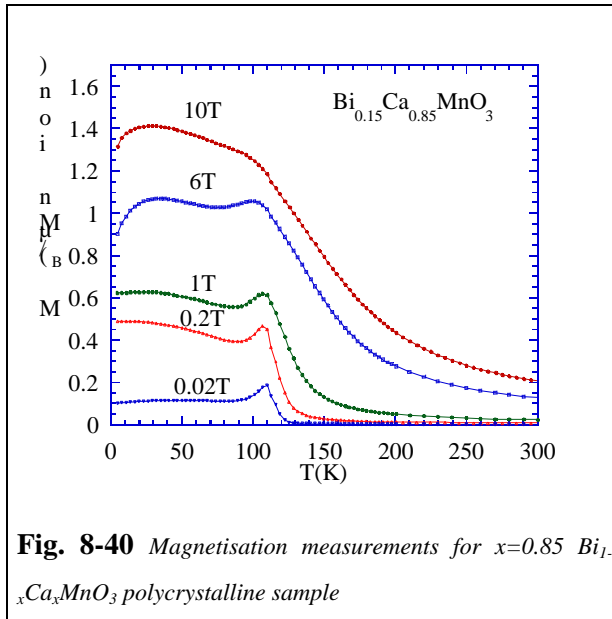
Fig. 8-39 *Magnetoresistance under 1T and 7T measured on x=0.85 and x=0.875 compounds.*
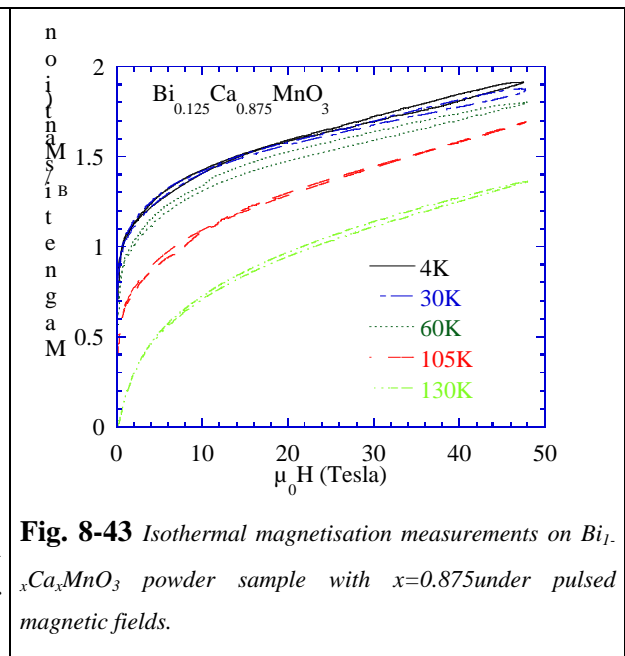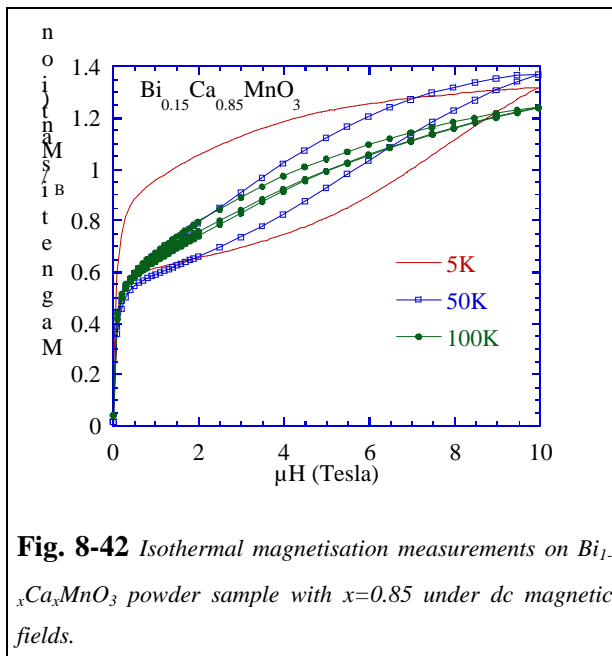
In Fig. 8-40 and Fig. 8-41 is shown the thermal evolution of the magnetisation measurements performed under several applied magnetic fields. Firstly, it can be observed that they do not evolve as most of the compounds exhibiting CO which present a drop of the magnetisation at the charge ordering temperature due to the change of the sign of the magnetic interactions. Contrarily, the compounds under study display a thermal evolution that reveals the competition between AFM and FM interactions. Under 10T of applied magnetic field, the magnetisation of the compounds is far from being the saturation magnetisations which were expected to be $3.85\mu_B/Mn$ (x=0.85) and $3.87\mu_B/M$ (x=0.875). In addition, magnetisation continues to increase upon the application of larger magnetic fields as can be observed from the measurements performed under high pulsed magnetic fields at SNCMP (Toulouse) on x=0.875 compound (Fig. 8-43). From the above measurements the spontaneous magnetisation of the x=0.875 compound is found to be $1.32(4)\mu_B/Mn$ at 4K.

M(H) curves also show that these compounds are not conventional ferromagnets because in addition to the non saturation even under 50T of applied magnetic field, they display a low remanence and coercive field. The x=0.875 compound displays M(H) behaviour very similar to what would be expected in a canted AFM structure, and it is different to the behaviour exhibited by x=0.85 sample. The x=0.85 compound presents hysteresis in the M(H) measurements while no evidence of magnetic hysteresis was found in x=0.875 compound (Fig. 8-42).

In addition, in the M(H) measurements the main difference between the two samples occurs at low applied magnetic fields. The x=0.85 exhibits comparably smaller magnetisation at 5K for low applied magnetic fields.
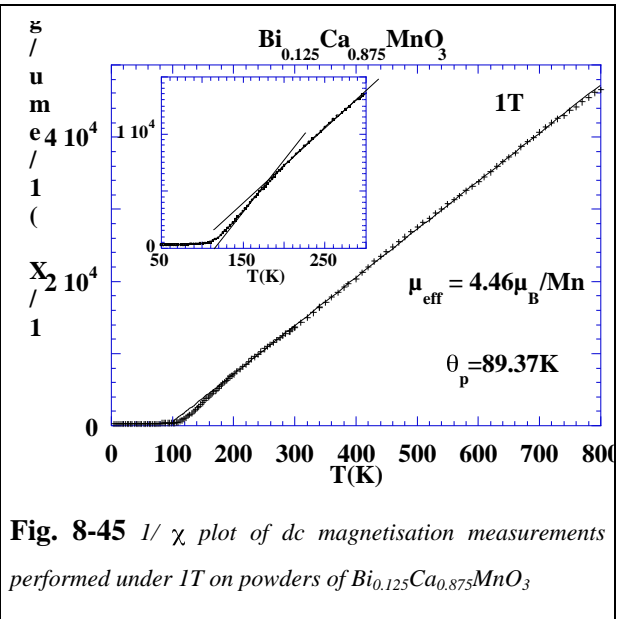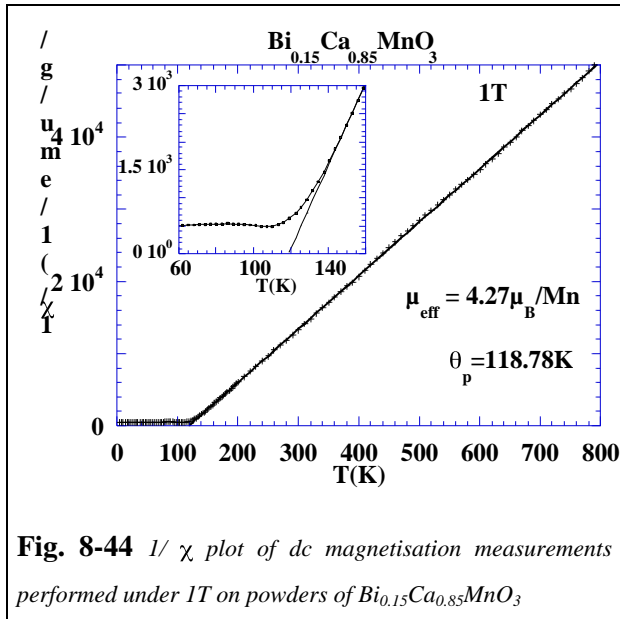
Fig. 8-40 *Magnetisation measurements for x=0.85 Bi$_{1-}$$_xCa_xMnO_3$ polycrystalline sample*

Fig. 8-41 *Magnetisation measurements for x=0.875 Bi$_{1-}$$_xCa_xMnO_3$ polycrystalline sample*

The magnetisation measurements of x=0.85 sample agree with saturation values reported in [227] under 1T of applied field at 5K. The author obtained M 0.5µ$_B$/Mn and we observed M 0.6µ$_B$/Mn for x=0.85 sample. For the x=0.875 sample Chiba et al gave M 1.15µ$_B$/Mn and we obtained 1.02µ$_B$/Mn. In x=0.85 compound a sudden increase has been reported in [225] and has been experimentally found in our samples (by M.Respaud at SNCMP (Toulouse)-private communication).

Fig. 8-42 *Isothermal magnetisation measurements on Bi$_{1-}$$_xCa_xMnO_3$ powder sample with x=0.85 under dc magnetic fields.*

Fig. 8-43 *Isothermal magnetisation measurements on Bi$_{1-}$$_xCa_xMnO_3$ powder sample with x=0.875under pulsed magnetic fields.*

Dc susceptibility measurements under 1T up to high temperatures (Fig. 8-44) show that the θ_p is larger for x=0.85 (θ_p =118K) sample than for x=0.875 (θ_p=89K), in agreement with what is expected

_____

due to the reduction of the density of e_g electrons in x=0.875, which will reduce the intensity of the DE FM interaction. The effective paramagnetic moment are very similar.

Fig. 8-44 *1/ χ plot of dc magnetisation measurements performed under 1T on powders of $Bi_{0.15}Ca_{0.85}MnO_3$*

Fig. 8-45 *1/ χ plot of dc magnetisation measurements performed under 1T on powders of $Bi_{0.125}Ca_{0.875}MnO_3$*

In conclusion, about $1\mu_B$/Mn spontaneous FM component is observed in heavily doped (x=0.85 and x=0.875) of $Bi_{1-x}Ca_xMnO_3$ compounds which is far from being the saturation value. More FM alignment of the Mn moments can be achieved under application of large magnetic fields indicating the existence of a sort of AFM and FM components in x=0.875 while a different behaviour is found in x=0.85.

The low values of the resistivity at low temperatures and the comparatively large values of the spontaneous magnetisation at low temperatures in both samples, suggest the lack of a CO state in these compounds. The semi-metal to insulator transitions observed in the resistivity measurements are associated to the development of a particular orbital ordering as will be shown in the following sections by the analysis of SXRPD and NPD data.

8.4.3 Phase segregation in $Bi_{0.15}Ca_{0.85}MnO_3$: Chemical heterogeneity

Ultrahigh resolution X-Ray powder diffraction, (SXRDP) and NPD are ideal tools for the study of phase segregation processes. On the one hand, NPD allows the study of the magnetic and nuclear structures and can give an indication of two-phase coexistence when there are two different types of magnetic structures with slightly different magnetic cell parameters. On the other hand, SXRPD, has good resolution (and narrow peaks) and permits to identify structures with similar cell parameters that coexist in a sample. Joint refinements (SXRPD and NPD) allow determining, with low error, the atomic positions and the composition of the phases, due to the different sensitivity of the techniques to heavy and light atoms and their different resolution.

216

Ultra-high resolution SXRPD patters were collected on BM16 powder diffractometer of ESRF (Grenoble, France) in Debye-Scherrer (transmission) configuration at 300K and 10K for the x=0.85 sample. The sample was introduced in a borosilicate glass capillary (=0.5mm) and rotated during the data collection. We used a short wavelength (0.442377(2) Å, E=28.03 keV) which was selected using a double-crystal Si(111) monochromator and was calibrated with Si NIST. A standard cryostat was used, which was compatible with using a beam size of about 7mm width and 0.7mm height. Measurements at each temperature were performed between 4 and 38 degrees (2).

NPD data was collected in D2B powder diffractometer at ILL (Grenoble, France) between 4K and 300K, in the high flux mode, selecting =1.594 Å wavelength. In addition, measurements using D20 powder diffractometer operating with =2.42 Å allowed having better resolution at low angles where the AFM peaks appeared and permitted to follow the thermal evolution of the cell parameters and magnetic structure.

8.4.3.1 Room temperature structure of $Bi_{0.15}Ca_{0.85}MnO_3$

At 300K, $Bi_{0.15}Ca_{0.85}MnO_3$ was found to be single-phase and the diffraction pattern was refined satisfactorily using the Pnma orthorhombic space group (a=5.32685(2), b= 7.50241(4), c=5.30110(3)). In Fig. 8-46 are shown the experimental and simulated powder diffraction patterns for SXRPD and NPD at 300K. The refinement was performed following the standard procedure: firstly scale factors and background parameters, afterwards the unit cell parameters, zero-shift error, peak shape coefficients and finally atom positions and temperature factors.

Small impurity peaks were found in SXRPD data and were identified as providing from $CaMn_2O_4$ phase which was found in a ratio of about 3.6(1)% in volume.

At RT the SXRPD refinement showed systematic errors associated to the peak shapes that were identified as coming from strain effects. Therefore, we used the Thompson-Cox-Hastings

Fig. 8-46 *SXRPD and NPD Rietveld plots of $Bi_{0.15}Ca_{0.85}MnO_3$ at 300K*
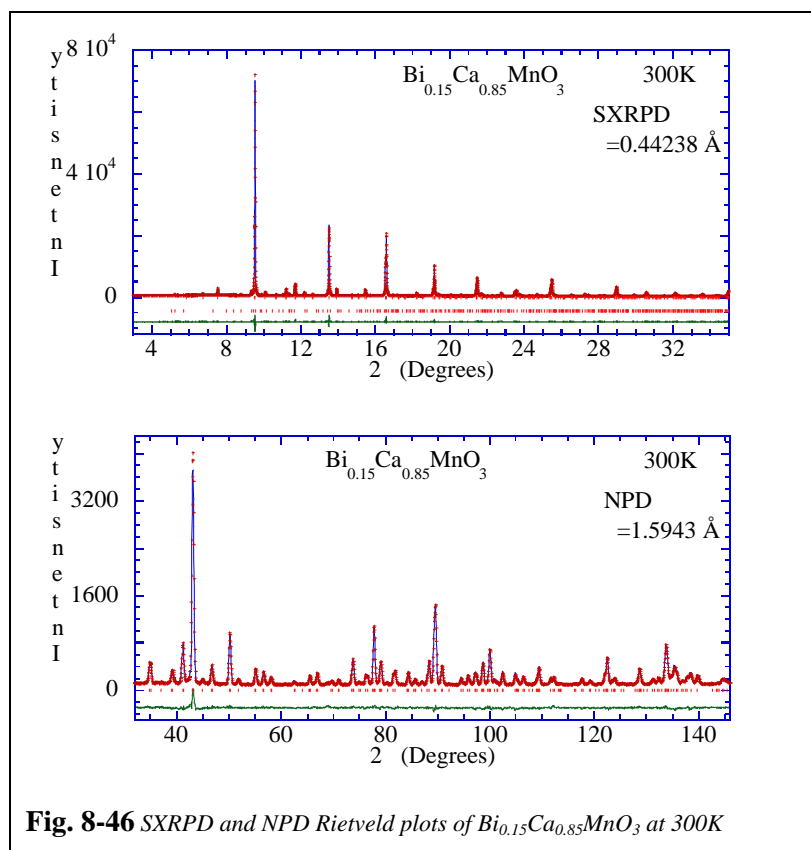
pseudo-Voigt peak shape type function, in FULLPROF software, in order to account for microstrains and size effects (this function is not convoluted with axial divergence asymmetry function but we did not observe relevant peak asymmetry). In this peak shape setting, there are six parameters characterising the peak shape: U, V, W, X, Y and IG. Additional parameters are added when a strain model is used. The parameters U,V,W take into account the instrumental contribution, while X is the isotropic Lorentzian strain parameter. The Y parameter permits to consider the anisotropic gaussian strain broadening when considering a special model for strain peak broadening. IG and SZ parameters take into account the isotropic gaussian and lorentzian grain size broadening. The main difference between the size and strain peak broadening is that while strain peak broadening has an angular dependence (tan( )), the size peak broadening effect is given by the Scherrer formula (1/cos( )).

At RT the FWHM of the SXRPD peaks of x=0.85 compound was dominated by sample dependent effects. The lowest FWHM value reported up to now using this experimental set-up at ESRF has been of 0.004° for $Na_2Ca_3Al_2F_{14}$ [236] and the FWHM for non overlapping peaks in our sample corresponding to the Bragg reflections (111) at 7.55° or (113) at 12.20° is about FWHM 0.023° and 0.024° respectively. Hence, the peaks are rather wide compared to the experimental resolution of the diffractometer.

The gaussian contribution to the peak shape was very small 0.1 $(0.01°)^2$ and the lorentzian contribution due to microstrains was rather high X 11(0.01°). No peak broadening due to crystallite size effects was observed. Therefore, the main effect contributing to the peak broadening is the Lorentzian contribution due to isotropic strain effects.

The origin of microstrain can be found in the existence of defects, or compositional fluctuations, which are the cause of the existence of a distribution of cell parameters within the sample. Regions with slightly different chemical composition can have slightly different cell parameters and contribute to the peak shape broadening when they have similar space group symmetry.

From joint refinements (SXRPD-NPD) we determined the cell parameters and atomic positions which are given in Tab. 8-XIV together with some selected distances and angles Tab. 8-XII.

The <Mn-O-Mn> bonding angle at RT in this compound is more straighten than in the x=2/3 compound (<Mn-O-Mn>(x=0.85)=157.3(1)°, <Mn-O-Mn>(x=0.66)=156.1(1)°). On the other hand the <Mn-O> mean distance is shorter than in the x=2/3 compound (<Mn-O>(x=0.85)=1.915(1)Å ,<Mn-O>(x=0.66)=1.938(3)Å) in accordance with the reduction of the Mn^{+3} proportion. In addition, at RT the oxygen octahedra are not very distorted ($_d$=10).

The refinements with the stoichiometric composition were satisfactory except for some small peaks that presented a lack of intensity. For that reason, we refined the occupation factor of the ions. Mn ion occupation fitting did not improve the refinement and the obtained value was very close to the

stoichiometric value. We also fitted independently without restrictions the occupation factors of Bi and Ca ions which gave the following results: Bi=0.168(2)% and Ca =0.76(1)%. In Fig. 8-47 and Fig. 8-48 it can be observed the difference in the SXRPD patterns when Bi and Ca occupancies are fitted at RT.

A central result is that, at RT, we found a single-phase diffraction pattern indexed with an orthorhombic (Pnma) space group exhibiting isotropic peak broadening associated to strain. In addition, the inspection of the Mn-O distances revealed the existence of a relatively regular MnO_6 octahedra. The joint refinement allowed the refinement of the composition and revealed a slight deficiency of Ca in the sample (8%) while Bi content was nearly the stoichiometric value.
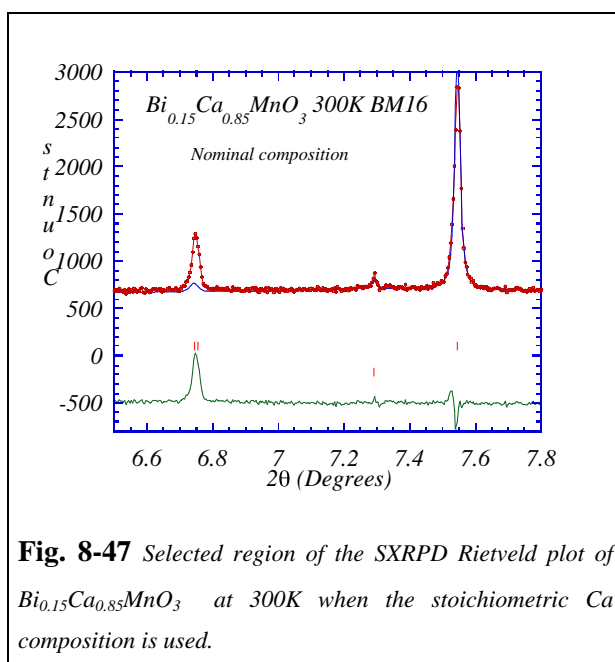

Fig. 8-47 *Selected region of the SXRPD Rietveld plot of $Bi_{0.15}Ca_{0.85}MnO_3$ at 300K when the stoichiometric Ca composition is used.*

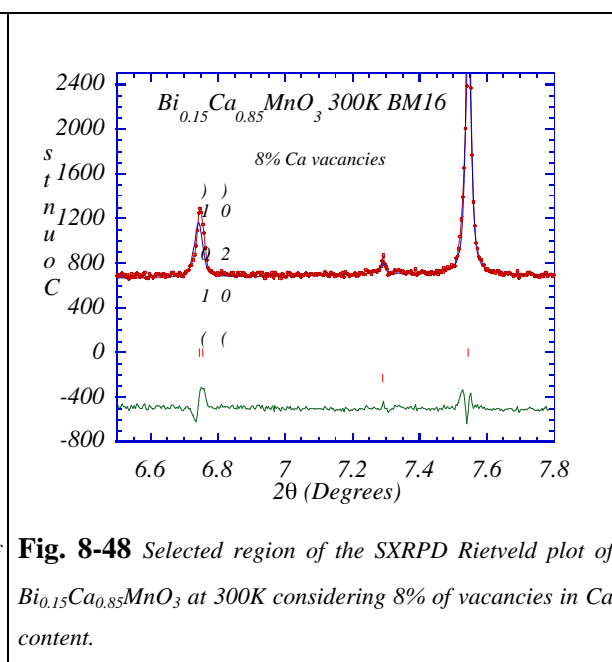**Fig. 8-48** *Selected region of the SXRPD Rietveld plot of $Bi_{0.15}Ca_{0.85}MnO_3$ at 300K considering 8% of vacancies in Ca content.*

8.4.3.2 Low temperature macroscopic phase coexistence

At 10K the diffraction pattern of $Bi_{0.15}Ca_{0.85}MnO_3$ is very complex. An indication of the complexity is shown in Fig. 8-49 where similar 2 range is shown for the 300K and 10K SXRPD patterns.

At low temperature there is macroscopic phase segregation. A detailed study permitted to conclude that the diffraction pattern consists in two phases. The majority phase (66%) has been identified as corresponding to $P2_1/m$ monoclinic symmetry (a=5.34132(4)Å, b=7.44276(4)Å, 5.30779(7)Å, =91.0807(7)°at 10K) and from now on will be referred as LT-M. The minority phase (30%) is a reminiscence of the HT Pnma orthorhombic phase (a=5.31931(7)Å, b=7.48097(8)Å, c=5.28282(7)Å) and in the following it will be referred as LT-O. This structural transition from Pnma to $P2_1/m$ symmetry has been already reported in other manganites [217, 237]. Preliminary structural
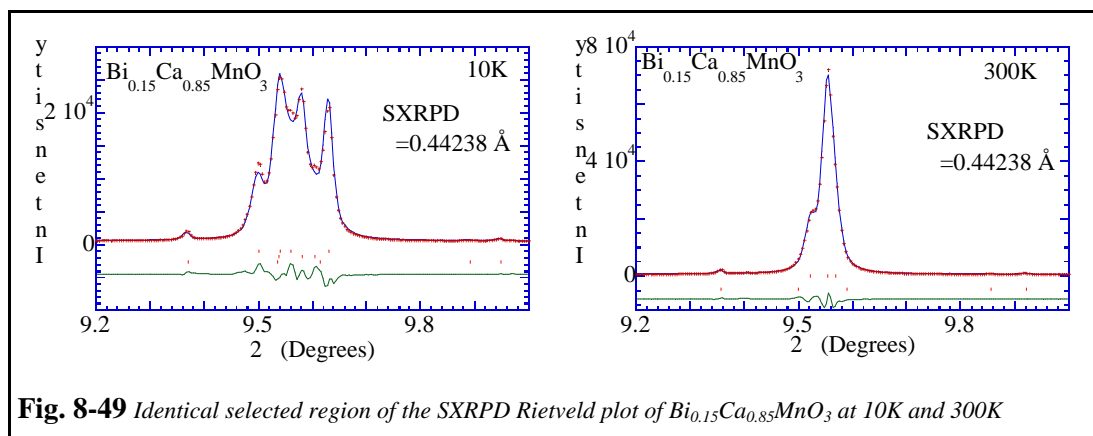
_____

Fig. 8-49 *Identical selected region of the SXRPD Rietveld plot of $Bi_{0.15}Ca_{0.85}MnO_3$ at 10K and 300K*

joint neutron and synchrotron refinement was performed excluding low angles in the neutron diffraction pattern (2θ >48°) in order to avoid antiferromagnetic peaks.

The analysis of the RT joint refinement of SXRDP and NPD displayed no evidence of phase coexistence. The only source of doubt could be found in the existence of isotropic peak broadening due to microstrain at RT. However, upon cooling, the sample exhibits a phase transition from the HT-O phase to LT-M phase coexisting with a LT-O phase. The thermal evolution of such transition has been studied by medium resolution NPD using D20 diffractometer at ILL (λ=2.24Å). D20 is a high-flux medium resolution powder-diffractometer equipped with a large-area linear curved position-sensitive detector (PSD) which allows fast NPD data acquisition. It is very convenient for temperature scans and with rather good low angle resolution that permits to determine magnetic structures and to follow their thermal evolution.

In Fig. 8-50 is presented the thermal evolution of a selected 2θ range of the NPD (D20) patterns. At the structural transition temperature, certain peaks exhibit a splitting characteristic of the orthorhombic to monoclinic structural transition. The splitting of the peaks is concomitant with the onset of long range AFM order.

The results of the Rietveld analysis using medium resolution NPD data also permitted to follow the thermal evolution of the cell parameters Fig. 8-51.
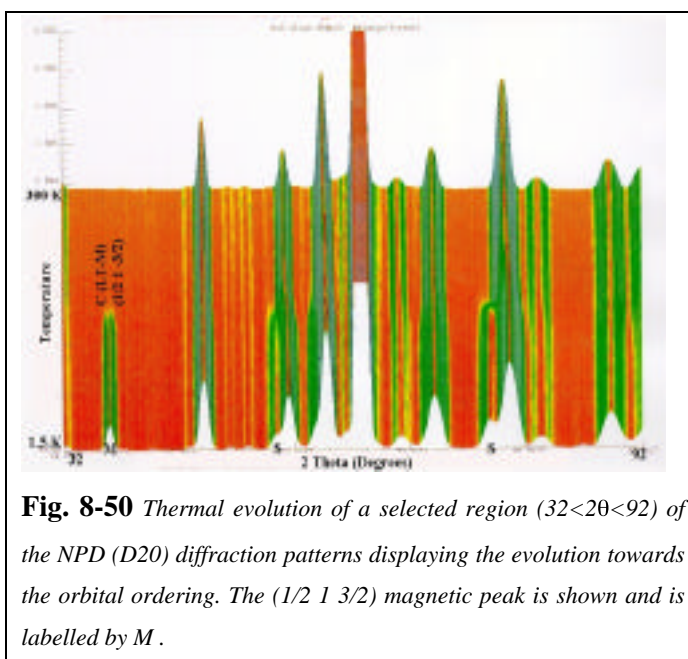

Fig. 8-50 *Thermal evolution of a selected region ($32<2\theta<92$) of the NPD (D20) diffraction patterns displaying the evolution towards the orbital ordering. The (1/2 1 3/2) magnetic peak is shown and is labelled by M .*
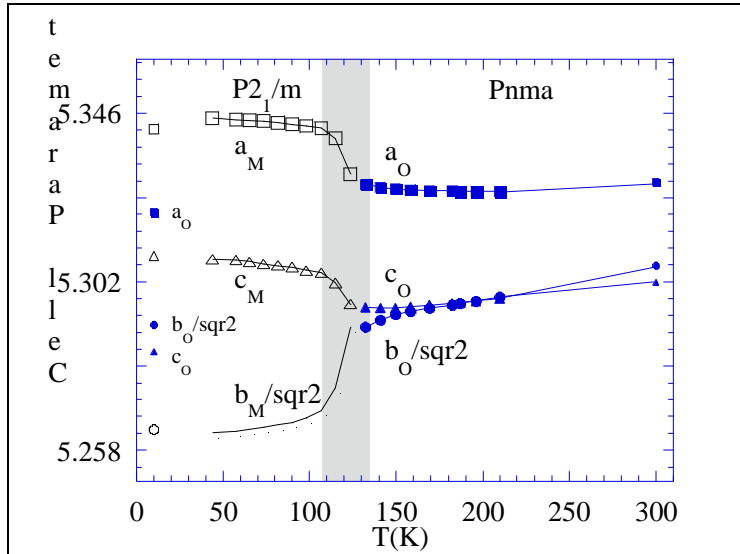
Fig. 8-51 *Thermal evolution of the cell parameters of the majority phase in $Bi_{0.15}Ca_{0.85}MnO_3$ as extracted from NPD Rietveld refinements*

The refinement was performed using two phases below the structural transition temperature (T_{OO}=125K) and one phase at RT. The LT-O phase cell parameters obtained from these refinements displayed large errors so only the majority phase cell parameters are shown.

The LT-O/LT-M phase fraction and low temperature cell parameters were kept fixed to the value obtained from joint refinements of high resolution NPD and SXRPD data at 2K and the neutron wavelength at 1.5K of D20 NPD pattern was refined. After this preliminary refinement, the cell fraction and cell parameters where kept free when refining at higher temperatures. Small symbols at 10K and 300K in Fig. 8-51, are the obtained values from joint refinements using high resolution SXRPD and NDP.

The anisotropic thermal evolution of the cell parameters (Fig. 8-51) strongly suggests the stabilisation of a particular orbital ordering while the orthorhombic phase do not show such anisotropic change. The temperature of the structural phase transition (T_{OO}=125K) coincides with the increase of the magnetisation (Fig. 8-40) and with the slope change of the resistivity measurements (Fig. 8-37).

When analysing the high-resolution SXRPD data a good description of the low temperature phases required the resolution of systematic discrepancies in the peak intensities associated to the peak shape. The analysis of the Bragg peak shape showed a marked anisotropic peak broadening in the monoclinic phase (LT-M) while the orthorhombic LT phase (LT-O) displayed lower peak broadening than at RT.

Using FULLPROF software we were able to simulate the anisotropic peak broadening of the monoclinic phase using uniaxial strain (strain model
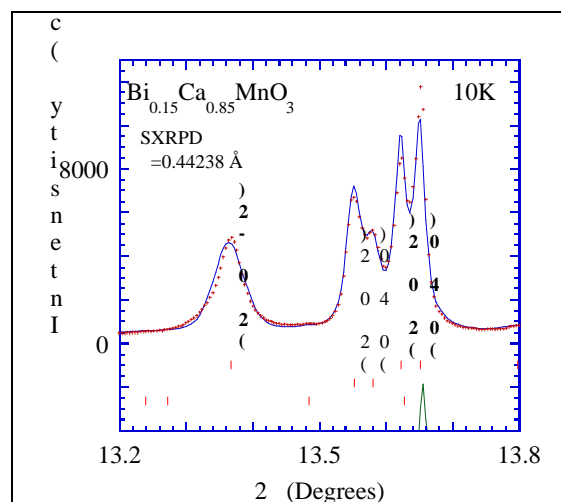

Fig. 8-52 *Rietveld plot at 10K of a selected area of the SXPD pattern showing one of the anisotropically broadened peaks of the monoclinic LT phase*

221

7) and a pseudo-voigt peak shape (shape function 7), being the direction of the strain the (1 0 –1) in the P 1 2_1/m 1 setting. The orthorhombic phase did not show anisotropic peak broadening and thus it was treated as at RT. The FULLPROF software used considers the anisotropic strain contribution to the peak shape to be gaussian. However in these samples, the anisotropic broadening is mainly lorentzian. A selected 2 range of the SXRPD pattern is shown in Fig. 8-52 where it can be noticed the large lorentzian peak broadening of the (2 0 –2) in contrast to the (2 0 2) Bragg peaks of the LT-M phase.

The standard peak shape parameters for the simulated SXRPD at RT and at 10K (LT) suggest that there dos not exist relevant gaussian peak broadening due to crystallite size (GS 0) at any temperature and there exist an increase of the gaussian isotropic peak broadening at low temperature ($U=U_{ins}+U_{strain}$) (Tab. 8-XI).

Tab. 8-XI. *Refined values of the peak shape parameters for SXRPD patterns of the powder sample $Bi_{0.15}Ca_{0.85}MnO_3$*

SXRPD peak shape parameters					
Temperature		U	X	Y	GS
RT		0.001(1)	0.108(1)	0.0061(6)	0.000
LT	M-LT	0.033(3)	0.065(2)	0.010(3)	0.000
	O-LT	0.044(3)	0.07(2)	0.007(2)	0.000

The orthorhombic phase displays a reduction of the isotropic lorentzian peak broadening due to strain (X) at LT. Therefore, our analysis suggests that the pristine orthorhombic phase at LT is less strained that at HT. This observation rules out the possibility of having two phase coexistence at low temperature due to the existence intragranular strain which enables the transition of a certain volume of the pristine phase as pointed out in other manganites [162].

The monoclinic phase develops an anisotropic peak shape broadening associated to the strain which manifests in the STR and Y parameter.

In conclusion, from the analysis of the peak shape we conclude that the high temperature orthorhombic phase (HT-O) display isotropic strains, which are released in the low temperature pristine orthorhombic phase (LT-O). In addition, the low temperature monoclinic phase (LT-M) shows large lorentzian strains in the (1 0 –1) direction. The existence of such strain can be satisfactorily explained considering the phase transition which occurs between the Pnma to P2_1/m. However, first of all we will focus on the origin of the two phase coexistence at low temperature.

_____

The stabilisation of the low temperature phase implies the localisation of the electrons and is associated to a semi-metal to insulator transition. Atomic positions, selected angles and bond distances of the majority and minority phases are given in Tab. 8-XIV and Tab. 8-XII.

The comparison of the Mn-O bond distances of the majority and minority phases at low temperature reveal anisotropic deformation in the LT-M phase. Upon cooling, the Mn-O apical distances contract by -0.93% in the LT-M phase while equatorial distances expand by 0.31%.

Slightly different oxygen octahedra associated to Mn1 and Mn2 is observed. However, the difference in the MnO_6 octahedra between non equivalent Mn ions in the monoclinic phase is so small that the existence of charge ordering in this compound is completely excluded. In addition, we did not observe any superlattice peak at low temperatures in NPD nor SXRPD data.

The differences between the LT-M and LT-O phases reveal the existence of a particular orbital ordering in the monoclinic phase. The orbital ordering is suggested from the large value attained by the octahedra distortion parameters $_d$ and in the LT-M phase (Tab. 8-XII).

In the LT-O phase, the apical Mn-O distances have been only reduced by 0.15% and the equatorial Mn-O distances are the same within the error.

Mn-O-Mn bonding angles, are more closed in the LT-O phase than in the LT-M phase. This fact can be related to the magnetic structure that will be presented in the following section.

As there is no evidence of Scherrer's size peak broadening in any of the phases, we conclude that both phases have similar grain sizes that have been estimated to be 1000Å.

In Tab. 8-XII we have included some data of the compound $Sm_{0.15}Ca_{0.85}MnO_3$ extracted from [217]. The first remark is that in the Sm based compound presents also phase separation with a majority phase corresponding to a monoclinic phase (a=5.3340(1), b=7.4432(2), c=5.3076(1), =91.062(2)) but constituting the 94% of the sample volume and only 6% of orthorhombic phase (a=5.1375(5), b=7.4826(9), c=5.2899(5)). The comparison of the Sm and Bi based compounds reveals that both low temperature phases are very similar. The majority phase in Sm based compound displays similar MnO_6 octahedra and Mn-O-Mn bond angle in the LT-M phase in Bi based compound.

These similarities contrast with our findings in the bismuth based compounds with lower Ca content, where large differences in the MnO_6 octahedra were observed when compared to Sm or La based compound of the same Ca content (x 2/3). However, in the x>2/3 compounds the proportion of Bi ions is highly reduced and thus the effects of its electronegativity are less evident.

In order to obtain the maximum information of the origin of the macroscopic phase segregation exhibited by this compound we refined the occupation of the Bi and Ca cations at low

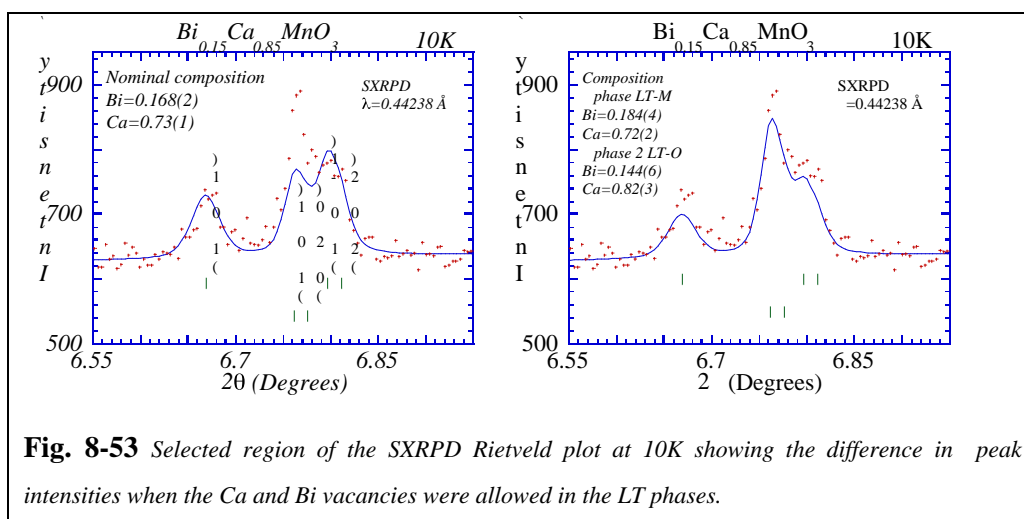temperature. This refinement was performed introducing also the magnetic contribution to NPD patterns.

Tab. 8-XII *Selected bond distances and angles in $Bi_{0.15}Ca_{0.85}MnO_3$ compound and reported values for $Sm_{0.15}Ca_{0.85}MnO_3$ extracted from* [217]

	$Bi_{0.15}Ca_{0.85}MnO_3$			$Sm_{0.15}Ca_{0.85}MnO_3$	
T(K)	10K		RT	*10K*	*RT*
	Pnma (30%)	P2$_1$/m (66%)	Pnma	*P2$_1$/m*	*Pnma*
$d_{Mn-O(1)}$ (Å)	**1.910(1)**	1.896(1) 1.893(1) **(1.895(1))**	**1.9129(5)**	*1.896(1) 1.897(1) (1.896(1))*	*1.909(0)*
$d_{Mn-O(2)}$ (Å)	1.898(5)	1.902(5) 1.905(5)	1.917(2)	*1.905(1) 1.904(1)*	*1.916(1)*
$d_{Mn-O(3)}$ (Å)	1.933(5)	1.944(5) 1.932(5)	1.914(2)	*1.932(2) 1.937(2)*	*1.917(1)*
d_{equat} (Å)	**1.916(5)**	Mn1=1.923(5) Mn2=1.918(5) **(1.921(5))**	**1.915(1)**	*1.919(2)*	*1.916(1)*
$\langle d_{Mn-O} \rangle$ (Å)	**1.914(3)**	1.914(3) 1.910(3) **(1.912(3))**	**1.915(1)**	*1.912(1)*	*1.914(1)*
φ_1=Mn-O1-Mn (deg)	**156.58(6)**	**158.84(5) 157.65(5)**	**157.33(2)**	*157.9(2) 157.7(2)*	*158.3(1)*
φ_2=Mn-O2-Mn (deg)	156.07(2)	156.8(2)	157.35(7)	*156.2(2)*	*157.1(1)*
φ_3=Mn-O3-Mn (deg)		157.3(2)		*157.8(2)*	
$< \varphi_{n--n}>$ (deg)	**156.24(4)**	**157.4(1)**	**157.34(4)**	*157.3(2)*	*157.5(1)*
$\sigma_d \times 10^4$	0.57	Mn1= 1.2 Mn2=0.7 (0.98)	0.08	*0.7*	*0.034*
$\varepsilon_d = \left\| \dfrac{d_{equat}}{d_{apic}} - 1 \right\| \times 10^4$	31	142 132	10	*126*	*36*
Bi1-O (Å)	2.571	2.337 2.323	2.534(2)		

We recall that the RT orthorhombic phase is not stoichiometric, and exhibits 8% of Ca vacancies as already mentioned. In the low temperature diffraction pattern, the refinement of the occupations was delicate because there are two coexisting phases strongly overlapped and because of the strong correlation between Debye-Waller (DW) temperature factors and occupation numbers. For that reason, we used the same DW factors for Bi and Ca in both LT phases and we fit the occupation numbers freely. Detailed analysis revealed that certain simulated peaks exhibit less intensity than experimentally measured and permitted us to determine the existence of differences in cation content between the coexisting phases as shown in Fig. 8-53

The results of the Bi and Ca cation refinement for the majority LT-M phase agreed with Bi=0.184(4)% and Ca=0.72(2)% while for the LT-O phase the result was Bi=0.144(6)% and Ca=0.82(3)%. These results were independently confirmed by Dr. M.A. G. Aranda using GSAS software for the analysis of present data.

_____

Hence, in contrast with the results reported by previous authors, the low temperature coexisting phases do not have the same stoichiometry. In fact, LT-O phase is nearly stoichiometric and the calcium vacancies are concentrated mainly in the LT-M phase. The different stoichiometry is the clue for the development of different orbital and magnetic structure at low temperature. If such a stoichiometry difference were not present, which would be the origin for the compound to exhibit two phase coexistence? In the next section, we will elucidate this question.

Fig. 8-53 *Selected region of the SXRPD Rietveld plot at 10K showing the difference in peak intensities when the Ca and Bi vacancies were allowed in the LT phases.*

Therefore, the main result from the high-resolution joint refinement is that the low temperature coexisting phases present different Ca content, being the Ca vacancies concentrated in the monoclinic phase.

8.4.3.3 Origin of the low temperature phase coexistence

Previously to this work, several origins for the macroscopic phase segregation process in these highly doped compounds have been considered:

i) One possibility could be the thermal diffusion of the species at the transition temperature from a homogeneous phase at RT. We ruled out this possibility in our compound because the particle size estimated from the Bragg peak width is consistent with grains larger than 1000Å which is incompatible with cation diffusion. In addition, the temperature at which the phase separation occurs (110K-130K) is too low to permit atomic diffusion to occur.

ii) Another possible origin of the macroscopic phase separation could be to consider that there exist an homogeneous phase at RT and when the structural transition takes place, large strains develop between nucleation centres of the low temperature phase (LT-M) and the pristine bulk material (O). These strains would not allow the whole sample volume to transform. This phenomenon is closely related to the martensitic phase transitions where metastable unchanged small domains coexist with the stable transformed phase. Such phase transition would imply to have a LT-O phase developing

_____

more strains than the RT phase which is not the case as shown in Tab. 8-XI. In our compound, the peaks of the LT-O phase are sharper than those of the HT-O phase and the peaks of the LT-M phase are anisotropically broadened (Fig. 8-52). Therefore, we conclude that phase coexistence at low temperature is not driven by intragranular strain effects.

iii) The most likely origin of the phase coexistence is that both phases coexist already at RT even if the high-resolution SXRPD pattern does not allow resolve the two phases. In this case, at RT we observe the averaged structure and composition. Upon cooling, each phase evolves in a different manner due to the development of orbital ordering. Hence, each phase develop the magnetic and orbital ordering that its composition requires. Such hypothesis allows explaining rather well the described results in these compounds.

In addition, Rietveld refinement of the LT pattern converged to different composition for the phases even considering the large errors existing due to strong peak overlap. Hence, the LT-M phase presents larger cation vacancies while the Ca content of the LT-O phase is the nominal.

Moreover, the compositional fluctuations existing in the sample are found to be at the origin of the development of microstrains. The microstrains present in the LT-M phase are very anisotropic. They can be understood as arising from dispersion of cell parameters and of monoclinic angle as sketched in Fig. 8-54. The dispersion of cell parameters at RT could be explained by compositional heterogeneity existent. However, at RT both phases seem orthorhombic, and upon cooling, one of the phases display electronic reorganisation and different orbital order than the other. The orbital order associated to the monoclinic phase is explained in the following section and is strongly correlated to the magnetic structure. It corresponds to the polarisation of the d_z^2 orbitals in the (1 0 –1) direction which corresponds to the Bragg reflections where the anisotropic peaks where observed.

The development of OO in one of the phases, origins anisotropic distortion of the cell parameters. The different thermal evolution of the cells originated by their particular OO, unmask the phase coexistence.

The origin of the existence of two different faces has been observed to be the existence of compositional fluctuations that have

Fig. 8-54 *Schematics of the origin of the anisotropic peak broadening*

been estimated to have a spatial width of about 1000Å. Hence, there will exist zones with averaged distortions in between the two phases (M and O) which probably exhibit a medium degree of distortion and thus are at the origin of the peak broadening at low temperature (Fig. 8-54).

226
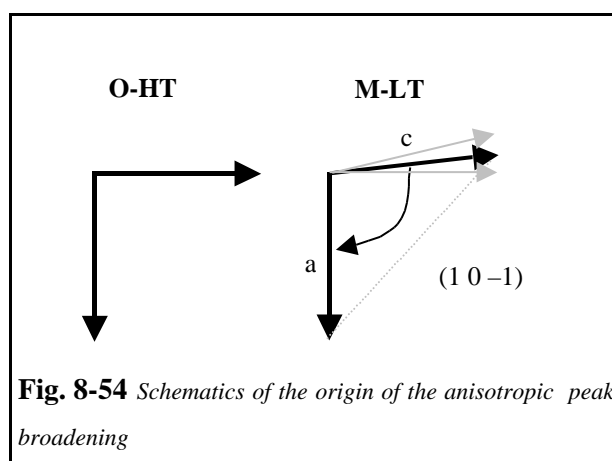
In conclusion, in $Bi_{0.15}Ca_{0.85}MnO_3$ compound we are facing to a macroscopic phase separation between two phases with slightly different Ca content and thus, different electronic density, which evolve differently upon cooling and develop different magnetic and orbital ordering.

8.4.3.4 Magnetic structures in $Bi_{0.15}Ca_{0.85}MnO_3$

We have analysed the magnetic order at low temperature in $Bi_{0.15}Ca_{0.85}MnO_3$ from the NPD data obtained using data from D20 and D2B at ILL.

In Fig. 8-55 can be observed the thermal evolution of the magnetic reflections in $Bi_{0.15}Ca_{0.85}MnO_3$ compound below 140K. Two sets of magnetic peaks were found at low temperatures associated to different structural lattices which corresponded to a C-type and a G-type AFM order (Fig. 8-55).

The C and G type magnetic structure were introduced in early works of Wollan and Khoeler [20]. The C-type magnetic structure corresponds to a magnetic order where the magnetic atoms have two FM and four AFM nearest neighbours. In this magnetic structure we find FM chains coupled AFM and, if no charge ordering exists, we would expect to have 1D electrical conduction.

The G-type magnetic structure corresponds to a magnetic order where every magnetic atom is surrounded by six neighbours coupled AFM to it. The pure G type magnetic structure characterises the $CaMnO_3$ compound containing only Mn^{+4} ions.

Inspection of Fig. 8-55 and Fig. 8-50 shows that: i) the apparition of C-type magnetic peaks coincides with the structural transition, ii) the magnetic peaks corresponding to the C or G type AFM structures do appear at similar temperatures (see (0 11) for G-type and (1/2 1 –3/2) for C-type)

In Fig. 8-56 are shown simultaneously the 10K and 300K low angles region of D20 pattern. At low temperature two sets of AF peaks develop which can be associated to a C
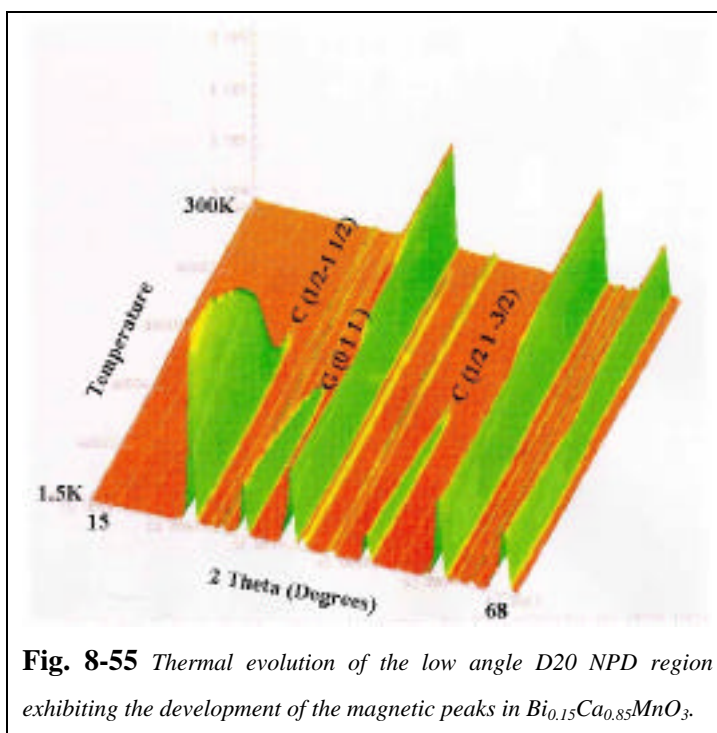
Fig. 8-55 *Thermal evolution of the low angle D20 NPD region exhibiting the development of the magnetic peaks in $Bi_{0.15}Ca_{0.85}MnO_3$.*

type ($2a \times b \times 2c$) and G type ($a \times b \times c$) magnetic structures (Pnma setting). The majority LT-M phase being associated to the C type magnetic structure while the LT-O phase is associated to the G type magnetic structure as extracted from the Rietveld refinement shown in Fig. 8-56b). In Tab. 8-XIII are

shown the propagation vectors of the magnetic structures as well as the refined magnetic moments for these phases.

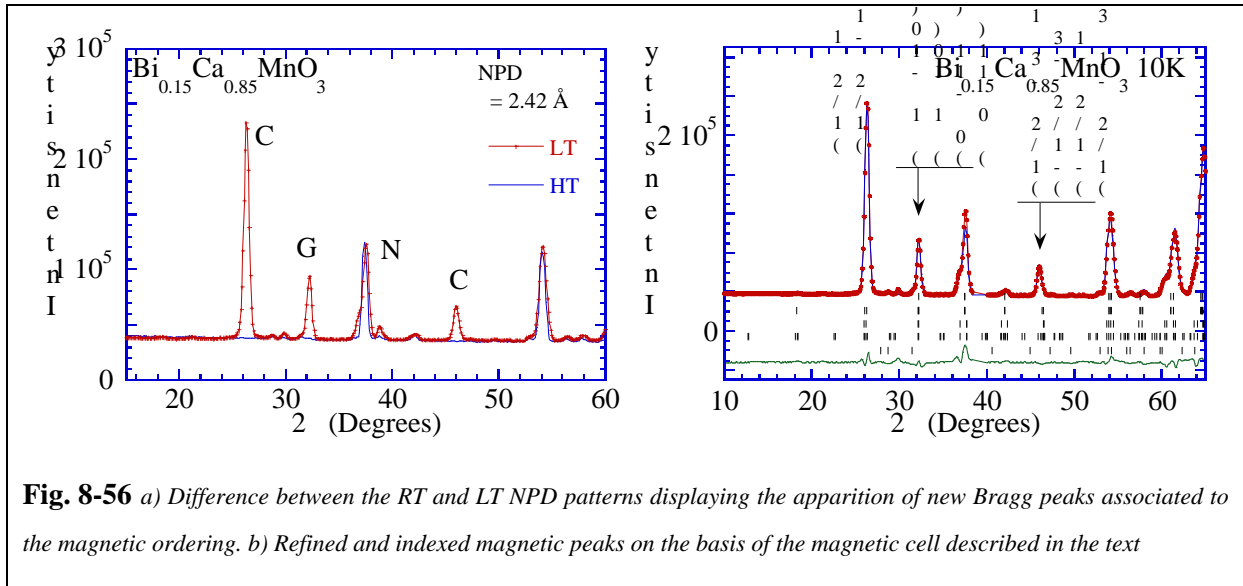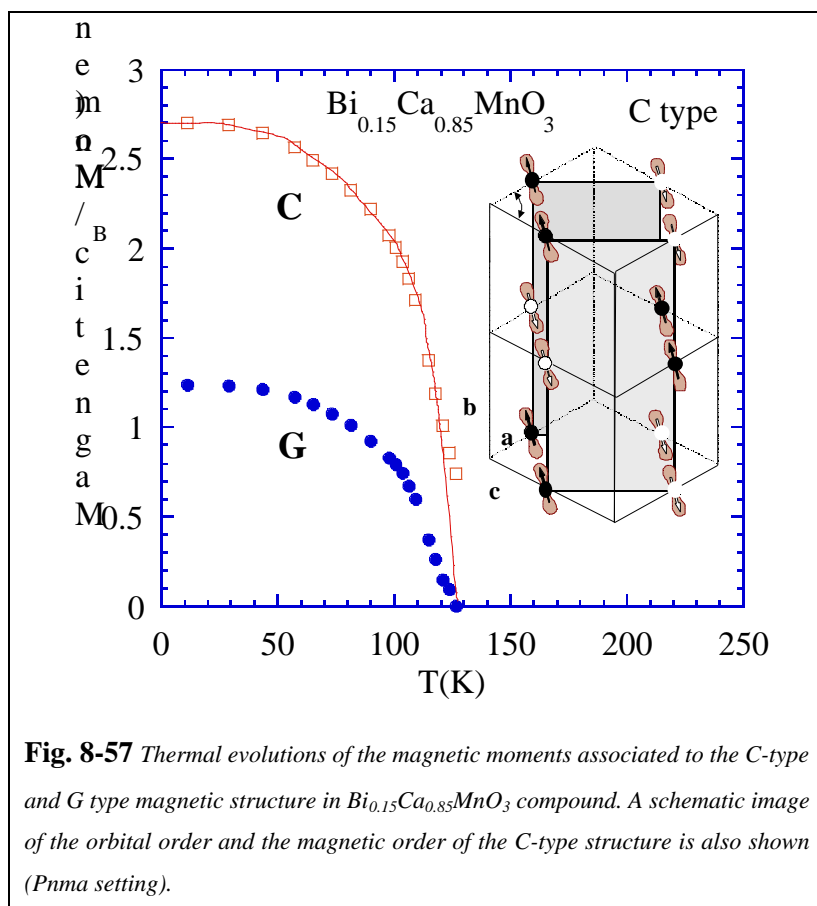| **Tab. 8-XIII** *Refined magnetic moments and propagation vectors in $Bi_{0.15}Ca_{0.85}MnO_3$ compound*		
x	0.85	
	Pnma	$P2_1/m$
k	(0,0,0)	(_ ,0,_)
Mn	(-,G_y,F_z)	(C_x,-,C_z)
m_x,m_y,m_z (μ_B)	0,1.21(3),1.04(6)	2.2(2),0,-1.8(3)
M_{tot} (μ_B)	1.58(5)	2.9(2)
$R_{f\text{-}mag}$	12	3.9

It is possible to establish a relationship between the magnetic order and the structural deformation presented in the above section. The minority phase at low temperature is the orthorhombic phase, it displays the nominal Ca content and develops a G type AFM structure.

The inspection of the Mn-O-Mn bond angles in the LT-O phase reveals that they are more bent than in the majority phase or RT phase. In addition, as it is the phase with larger Ca content (it showed the nominal composition), the number of Mn^{+3} is thus reduced when compared with the secondary LT-M phase and thus it seems natural to expect a G-type magnetic structure.

Fig. 8-56 *a) Difference between the RT and LT NPD patterns displaying the apparition of new Bragg peaks associated to the magnetic ordering. b) Refined and indexed magnetic peaks on the basis of the magnetic cell described in the text*

In the LT-M phase, there exist Ca vacancies and thus we expect to have larger Mn^{+3} content than the nominal composition. The introduction of e_g carriers permits de development of the DE interaction and an orbital ordering promotes the 1D FM in chains which are coupled AFM in the LT-M phase. The differences in the magnetic ordering between the coexisting low temperature phases can then be related to the different Ca content and thus to the different Mn^{+4}/Mn^{+3} ratio.

The development of the orbital order associated to the C type magnetic structure induces the cell distortion and drives orthorhombic to monoclinic phase transition which unmask the phase coexistence (Fig. 8-57).

Fig. 8-57 *Thermal evolutions of the magnetic moments associated to the C-type and G type magnetic structure in $Bi_{0.15}Ca_{0.85}MnO_3$ compound. A schematic image of the orbital order and the magnetic order of the C-type structure is also shown (Pnma setting).*

In addition, as the Mn ions in the chains are FM coupled, the e_g electrons could move freely within the chains propagating the FM interaction by DE if no charge ordering phenomena exists. In this sense, several observations make us conclude that there does not exist charge ordering in this compound: i) no superlattice peaks were found in SXRPD associated to large structural modulations that would be expected at this doping levels. ii) The resistivity at low temperatures in this compound is rather low when compared with CO compounds like x=1/2 or x=2/3.

The refinement with equal magnetic moments for the two unequivalent Mn sites in the monoclinic C-type AFM ordered phase converged to the values: Mn(1)=Mn(2)= 2.9(2)μ_B/Mn. And the G-type AFM component was found to be about 1.2 μ_B/Mn along the *b* direction (Pnma setting)

Similar orbital and magnetic order was also found in the reported monoclinic phase of the $Sm_{0.15}Ca_{0.85}MnO_3$ compound [217].

8.4.3.5 Origin of the weak ferromagnetism at low temperature

There is still an unsolved point concerning the magnetic order in $Bi_{0.15}Ca_{0.85}MnO_3$ compound. It is related to the evidence of weak ferromagnetism (spontaneous magnetisation $1\mu_B$/Mn at 5K) in magnetisation measurements (Fig. 8-42), which is not reflected in the pure C or G type magnetic structures given above.

Similar weak FM has been found in the parent compound $CaMnO_{3-}$ when 0.00 indicating that the introduction of electrons in the $[Mn^{+4}O^{-2}_3]$ non distorted framework diminishes the electrical resistivity and induces a semi-metallic like behaviour at temperatures above T_N [235].

Recent studies on highly hole doped compounds ($Sm_{1-x}Ca_xMnO_3$) with x 0.9 revealed the existence of a cluster glass FM state at low temperatures as extracted from electrical resistivity, thermoelectric power, thermal conductivity and magnetic measurements [213]. In addition in the NPD studies on $Sm_{0.15}Ca_{0.85}MnO_3$ compound, the authors reported that no clear evidence for FM components in the magnetic structure could be extracted from NPD data thus leading to the conclusion of the existence of FM clusters in the AFM matrix [217].

However the question is still unsolved, where the weak FM comes from?

There exist several hypotheses:

a) The weak FM comes from a canting of the G type magnetic structure;

b) The weak FM comes from a cluster glass state;

c) There exist electronic phase segregation and there exist FM domain inside a G-type AFM matrix.

First of all, it is important to recall that it has been theoretically predicted that in DE systems there exist a clear tendency favouring the phase separation versus the canted spin state [238]. Experimentally, it has been proved in the lightly doped hole regime on $La_{1-x}Ca_xMnO_3$ compound [203]. We have performed further analysis using joint refinement of high resolution SXRPD and NDP (D2B) which allowed determining the existence of a long range FM associated to the LT-O phase. Such FM component was introduced as a canting of the G type structure in the *c* direction on the Pnma setting. In

Fig. **8-58** is shown a comparison of different refinements of the NPD pattern when considering: a) FM component in G type structure (m_{FM} $1\mu_B$/Mn), b) No FM component added the G type structure. The best refinement is obtained when adding a FM component to the G type structure of about $1\mu_B$/Mn ion (Fig. 8-59).

230

A relevant issue, concerning the existence of FM moment in the orthorhombic phase is that the FM intensity does not arise as diffuse scattering which would mean the existence of small FM clusters but it arises as long range FM order which diffracts coherently at a certain Bragg reflection. This fact rules out the hypothesis b) of weak FM coming from cluster glass state or small FM clusters.
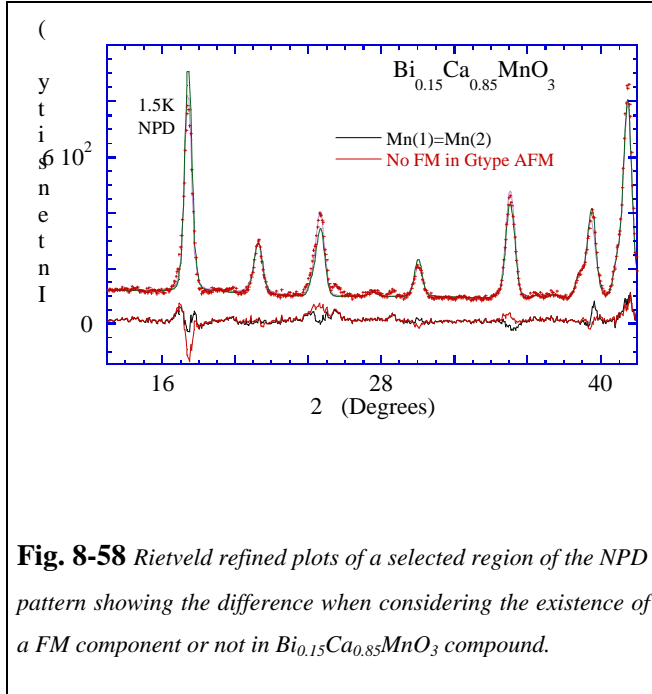

Fig. 8-58 *Rietveld refined plots of a selected region of the NPD pattern showing the difference when considering the existence of a FM component or not in $Bi_{0.15}Ca_{0.85}MnO_3$ compound.*
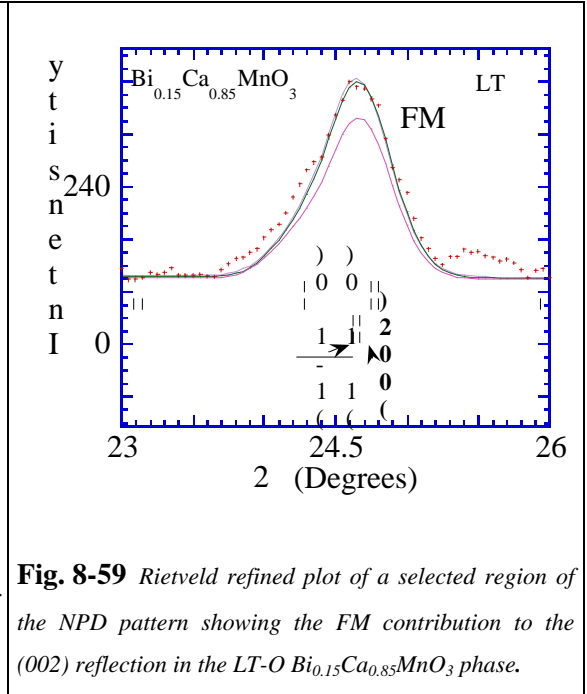

Fig. 8-59 *Rietveld refined plot of a selected region of the NPD pattern showing the FM contribution to the (002) reflection in the LT-O $Bi_{0.15}Ca_{0.85}MnO_3$ phase.*

In Fig. 8-60 is shown the thermal evolution of the integrated intensity associated to the (020)(101)(-101) reflections of the orthorhombic phase. It can be observed that below 150K a structural transition takes place and there is the splitting of the orthorhombic peaks leading to the LT-monoclinic phase. The Pnma to $P2_1/m$ phase transition can also be identified by the apparition of the monoclinic (10-1) peak. A remarkable finding is that below 100K the integrated intensity of the (10-1) monoclinic peak remains constant while the orthorhombic peak exhibits a gradual increase upon cooling and exhibits a saturation at about 60K. This increase of the integrated intensity in the orthorhombic low temperature phase is associated to the development of the FM.

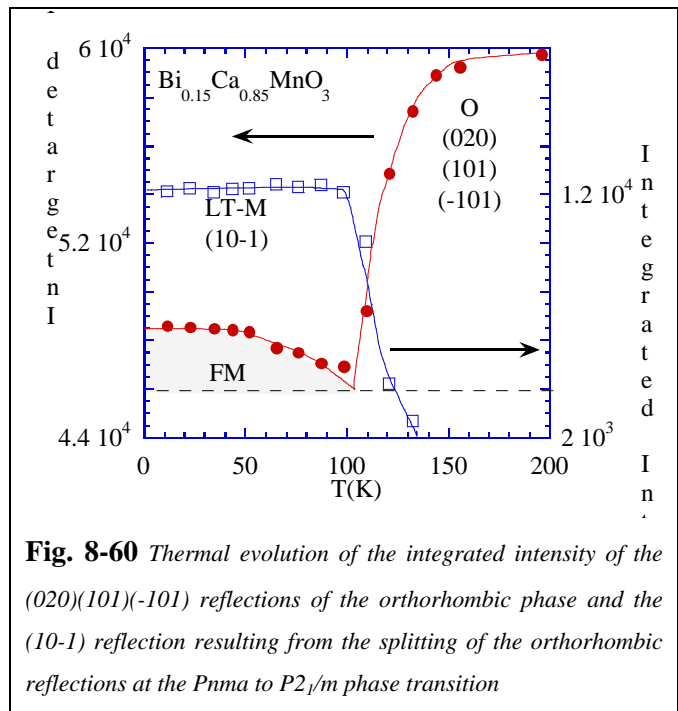However there are two possible configurations which could give rise to this

Fig. 8-60 *Thermal evolution of the integrated intensity of the (020)(101)(-101) reflections of the orthorhombic phase and the (10-1) reflection resulting from the splitting of the orthorhombic reflections at the Pnma to $P2_1/m$ phase transition*

_____

FM intensity: a canted state of the G type AFM structure or the existence of FM domains with the same orthorhombic cell than the G type phase. The latter case would be analogue to the low temperature ground state of $Pr_{2/3}Ca_{1/3}MnO_3$ compound described in detail in chapter 7.

Magnetic measurements revealed the existence of a small spontaneous magnetic moment below T_N (Fig. 8-42). M(H) hysteresis loops at 5K on this sample (Fig. 8-42) reveal the existence of about $0.6\mu_B/Mn$ of net moment under 0.5T of applied field and the existence of hysteresis. The existence of hysteresis reveals the existence of a non reversible magnetic state under the application of an external magnetic field. In addition, such irreversibility can not come from the signal of the majority C-type monoclinic phase because the x=3/4 compound which has a pure C-type magnetic structure did show straight M(H) curves under the measured magnetic fields, no spontaneous magnetisation at any temperature, no hysteresis, and no evidence of MR.

We suggest that the weak FM appearing in $Bi_{0.15}Ca_{0.85}MnO_3$ has its origin in the existence of FM domains in the G type AFM orthorhombic phase. These findings are corroborated by unpublished NMR data on $Pr_{1-x}Ca_xMnO_3$ samples with x<0.1[205].

In addition, the FM interaction in these regions should be governed by DE interaction because the application of an external magnetic field reduces the electrical resistivity by several orders of magnitude giving rise to MR.

The large values of the MR obtained can be understood based on a percolation system. When, no magnetic field is applied, the FM regions are not connected an the resistivity of the system is high. The application of a magnetic field of some Tesla, allows the connection between the FM regions, percolative type conduction takes place and the electrical transport behaviour turns to metallic.

In agreement with this explanations is the existence of bump at 80K in the electrical resistivity of the x=0.85 sample. The inspection of Fig. 8-60 reveals that FM alignment saturates below 60K and thus at 80K even if the application of an external magnetic field succeeds in reducing the resistivity by several orders of magnitude, the drop in the resistivity cannot be as large as in the temperature region were FM is rather well stabilised (T<60K)

8.4.3.6 Conclusions

Macroscopic phase segregation was observed below 125K in $Bi_{0.15}Ca_{0.85}MnO_3$. High resolution SXRPD and NPD experiments, confirmed that the $Bi_{0.15}Ca_{0.85}MnO_3$ compound displays macroscopic phase coexistence at all temperatures. Nevertheless, phase coexistence is only detected using high resolution SXRPD and NPD below the O(Pnma)$\rightarrow$M(P2$_1$/m) structural transition temperature due to the unmasking effect produced when the orbital order develops in one of the phases.

A relevant finding of this study is that the coexisting phases have slightly different calcium content. The LT-Monoclinic phase (66%) was found deficient in calcium while the LT-Orthorhombic phase (30%) was found to have the nominal composition.

In addition, the LT-Monoclinic phase exhibits C-type magnetic order associated with the polarisation of the d_z^2 orbitals along the (1 0 –1) direction. The absence of superlattice peaks and the low value of the electrical resistivity when compared to CO compounds of the same series as x=1/2 or x=1/3 lead us conclude that the ordering of the charges is not stabilised in the C-type structure.

The LT-Orthorhombic phase displays G-type magnetic ordering and does not contain Ca vacancies.

The origin of the MR exhibited by this compound has been found to be related to the weak FM present at low temperature. In this sense MR could not be associated to the monoclinic C-type phase because the compound x=3/4 was found to be purely C-type and no evidence of FM nor MR was found.

The origin of the weak FM at low temperatures was also analysed on the light of the results obtained from joint refinements of high resolution NPD and SXRPD data. The analysis permitted to find FM intensity in certain nuclear Bragg peaks of the orthorhombic low temperature phase. This remarkable finding allows concluding that FM in $Bi_{0.15}Ca_{0.85}MnO_3$ comes from large FM domains immersed into the G type orthorhombic phase.

The large value of the MR attained by this compound at low temperatures has been interpreted in the light of our results as arising from percolative type conduction in the sense that when no magnetic field is applied. The FM regions are not connected and the macroscopic behaviour of the compound is insulating. The application of a magnetic field will order the FM domains allowing the FM polarisation through the AFM G type ordered matrix and opening percolative paths for the electrical conduction between the FM domains. The FM interaction may be mediated by the DE interaction and once the FM domains are connected, the electrical behaviour is the characteristic of the percolative FM and metallic path and thus the compound display metallic conductivity. However, at such low magnetic field (about 5T for example) the saturation magnetisation of the compound is far from being attained as observed from magnetisation measurements but the electrical conduction shows a metallic like behaviour.

In the following section the compound with calcium composition x=0.125 is studied as a comparison with the x=0.85 compound which will help to go further in the understanding of macroscopic phase coexistence and MR in the highly doped regime.

Tab. 8-XIV Refined structural parameters and reliability factors for $Bi_{1-x}Ca_xMnO_3$, x=0.85 and 0.875.

x		0.85			0.875	
T(K)		10K	300K		10K	300K
	Pnma	P2$_1$/m	Pnma	Pnma	P2$_1$/m	Pnma
Fraction (%)	30%	66% (+3.5%CaMn$_2$O$_4$)		77%	15% (+7%CaMn$_2$O$_4$)	
a (Å)	5.31931(7)	5.34132(4)	5.32685(2)	5.31609(4)	5.3050(6)	5.3203(1)
b (Å)	7.48097(8)	7.44276(4)	7.50241(4)	7.47987(6)	7.4496(6)	7.4967(2)
c (Å)	5.28282(7)	5.30779(4)	5.30110(3)	5.28189(4)	5.3530(5)	5.2967(1)
β (deg)	90	91.0807(7)	90	90	90.833(8)	90
ε$_b$	2.11	11.59	1.68	1.87	11.5	1.41
Bi/Ca x	0.0378(3)	-0.0347(4)	0.03400(8)	0.0378(1)	0.007(7)	0.0336(2)
y	0.25	0.25	0.25	0.25	0.25	0.25
z	-0.0067(6)	0.0047(4)	-0.0056(2)	-0.0052(4)	-0.066(8)	-0.0048(6)
B (Å^2)	0.09(2)	0.10(2)	0.50(1)	0.2		0.73(2)
Bi/Ca x		0.4636(4)			0.482(6)	
y		0.25			0.75	
z		0.4911(4)			0.510(5)	
B (Å^2)		0.10(2)			0.2	
Mn1 x	0.00	0.50	0.00	0.00	0.00	0.00
y	0.00	0.00	0.00	0.00	0.00	0.50
z	0.500	0.00	0.50	0.50	0.50	0.00
B (Å^2)	0.20(5)	0.11(3)	0.46(3)	0.2	0.2	0.40(2)
Mn2 x		0.00			0.50	
y		0.00			0.00	
z		0.50			0.00	
B (Å^2)		0.11(3)			0.2	
O1 x	0.484(1)	0.012(1)	0.4881(3)	0.4872(8)	0.54(1)	0.487(1)
y	0.25	0.25	0.25	0.25	0.25	0.25
z	0.072(1)	0.565(1)	0.0699(5)	0.082(1)	-0.06(1)	0.072(1)
B (Å^2)	0.6(1)	0.3(1)	0.60(3)	0.2	0.02	0.5(1)
O2 x	0.2864(8)	0.493(1)	0.2877(2)	0.2895(6)	0.02(1)	0.2887(9)
y	0.0358(6)	0.75	0.0329(2)	0.0339(5)	0.75	0.0310(8)
z	0.7083(9)	0.069(1)	0.7123(3)	0.7109(7)	0.55(1)	0.714(1)
B (Å^2)	0.63(7)	0.01(9)	0.54(2)	0.2	0.3	0.5(1)
O3 x		0.7136(8)			0.253(8)	
y		0.0357(7)			0.01(1)	
z		0.286(9)			0.679(4)	
B (Å^2)		0.60(7)			0.2	
O4 x		0.7889(9)			0.73(1)	
y		0.5338(6)			0.51(1)	
z		0.788(1)			0.777(7)	
B (Å^2)		0.62(7)			1.02	
Ocupation	Bi(x)=0.138(6) Ca(x)=0.84(3)	Bi(x)=0.198(4) Ca(x)=0.67(2)	Bi(x)=0.168(2) Ca(x)=0.76(1)			
Reliability Factors	RF(X)=2.8 RF(N)=8.5	Rwp(X)=5.23 Rwp(N)=7.15	RF(X)=3.7 RFNeut=4.8			
R_f (%)	3.01	3.62	3.71	6.72	16.8	4.02
χ^2		6.24	4.34		5.43	19.7

_____

8.4.4 The low electron doped regime: $Bi_{0.125}Ca_{0.875}MnO_3$

A similar SXRPD and NPD study presented in the previous section has been carried out on $Bi_{0.125}Ca_{0.875}MnO_3$ compound. The main objective is to determine the ground state in this compound getting insight into the macroscopic phase segregation phenomena and to investigate the origin of the lower value of the magnetoresistance.

8.4.4.1 Structure of $Bi_{0.125}Ca_{0.875}MnO_3$: A neutron and synchrotron study

The SXRPD and NPD (D20) study of the sample $Bi_{0.125}Ca_{0.875}MnO_3$ reveals that the compound shows strong similarities with the x=0.85 sample. The lack of high resolution NPD data did not allowed us to perform joint SXRPD and NPD refinements in this compound. Nevertheless, similar analysis of the lattice distortion and phase coexistence can be performed accepting the limitations of SXRPD technique for light atom position determination.

SXRPD diffraction data at RT on x=0.875 compound displays a single phase diffraction pattern indexed on the basis of the Pnma space group (a= 5.3203(1) Å , b=7.4967(2)Å , c=5.2967(1)Å). In Tab. 8-XIV are shown the refined lattice parameters and atomic positions obtained from the RT refinement. Oxygen positions display large errors because of the small X-Rays diffusive power of oxygen. Within the error, the MnO_6 octahedra is nearly regular as in the case of the x=0.85 compound. Selected distances and angles are shown in Tab. 8-XV.

Upon cooling, it is evidenced a macroscopic phase separation process at T 120K, similar to that for the x=0.85 sample. In this case, a minority (15%) monoclinic phase which has a $P2_1/m$ space group (a=5.3050(6)Å, b=7.4496(6)Å, c=5.3530(5)Å, =90.833(8)°) coexist with a majority orthorhombic Pnma phase (77%) (a=5.31609(4)Å, b=7.47987(6)Å , c=5.28189(4)Å). Rietveld plots of the RT and low temperature SXRPD patterns are shown in Fig. 8-62. No composition refinement has been carried out in this case because of the lack of high-resolution NPD patterns.

The thermal evolution of the cell parameters has been analysed from D20 NPD data. In Fig. 8-61 is shown the thermal evolution of the majority orthorhombic phase cell parameters. The obtained values of the low temperature and RT cell parameters of the minority monoclinic phase extracted from high resolution SXRPD data are also shown.

It should be pointed out the large difference in the thermal evolution of the cell parameters of the two phases. The majority orthorhombic phase displays very small anisotropic thermal evolution of the cell parameters when compared to the monoclinic minority phase. Similar to the behaviour observed in x=0.85 sample as shown in Fig. 8-51.
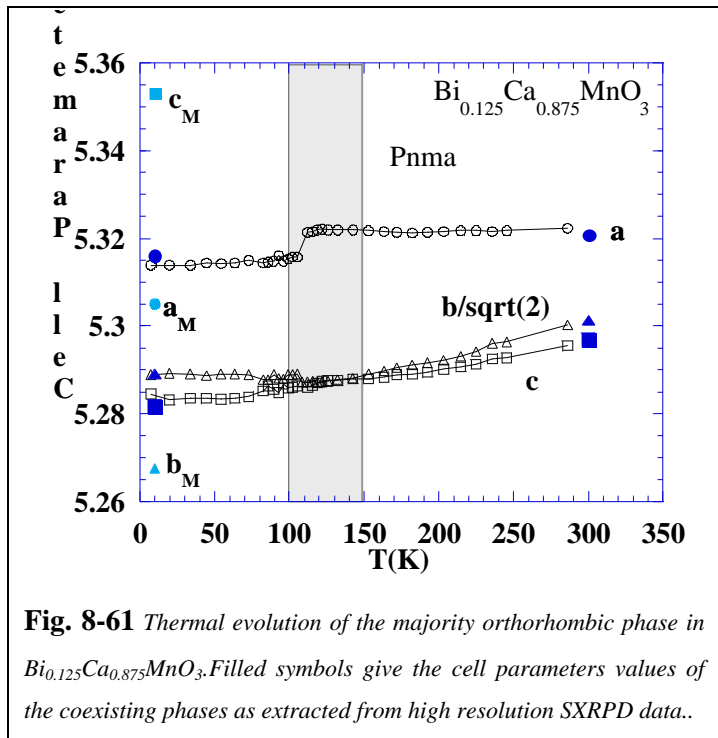
Tab. 8-XV *Selected bond distances and angles in* $Bi_{0.125}Ca_{0.875}MnO_3$ *compound*

| T(K)	10K		RT
	Pnma	$P2_1/m$	Pnma
$d_{Mn-O(1)}$ (Å)	1.921(1)	1.88(1) 1.90(1)	1.914(2)
$d_{Mn-O(2)}$ (Å)	1.916(3)	1.64(3) 2.14(3)	1.924(5)
$d_{Mn-O(3)}$ (Å)	1.910(3)	2.07(4) 1.72(4)	1.899(5)
d_{equat} (Å)	1.913(3)	1.86 1.93 (1.895)	1.912(5)
$\langle d_{Mn-O}\rangle$ (Å)	1.916(3)	1.86 1.92 (1.89)	1.912(4)
$_1$=Mn-O1-Mn (deg)	153.46(6)	156.1(6) 161.6(4)	156.67(8)
$_2$=Mn-O2-Mn (deg)	156.6(1)	161(1)	158.1(2)
$_3$=Mn-O3-Mn (deg)		176(2)	
< n-O-Mn> (deg)	155.55(8)	162(1)	157.6(1)
$_d \times 10^4$	0.05		0.29
$\left\|\dfrac{d_{equat}}{d_{apic}}-1\right\| \times 10^4$	10	79 26	10
Bi1-O (Å)	2.5187	2.643 2.61	2.533

The orthorhombic distortion of the unit cell can be quantified through the $_b$ parameter defined as $\varepsilon_b = \left|1 - \dfrac{\sqrt{2}b}{(a+c)}\right|10^3$. When comparing the value for the x=0.85 ($_b$(LT-M)=11.59 and $_b$(LT-O)=1.69) and x=0.875 ($_b$(LT-M)=11.51 and $_b$(LT-O)=1.87), it suggests that we are dealing with the similar phases in the two compounds.

In addition, the inspection of the RT and LT cell parameter change ($_a$=(a$_{LT}$-a$_{RT}$) 10^3/a$_{LT}$) revealed that the

Fig. 8-61 *Thermal evolution of the majority orthorhombic phase in* $Bi_{0.125}Ca_{0.875}MnO_3$.*Filled symbols give the cell parameters values of the coexisting phases as extracted from high resolution SXRPD data..*

HT-O to LT-O exhibit very similar evolution upon cooling in x=0.85 and x=0.875 compounds for the three cell parameters ($_a$(x=0.85)=-1.41, $_b$(x=0.85)=-1.41, $_c$(x=0.85)=-3.44 and ($_a$(x=0.875)=-0.79, $_b$(x=0.875)=-2.24, $_c$(x=0.875)=-2.79). This supports that the low temperature orthorhombic and monoclinic phases respectively correspond to the same phases in both samples. Only the values

obtained in the *a* and *c* directions of the monoclinic phase which are more sensitive to the C orbital order, differ from one sample to the other ($_a$(x=0.85)=2.71, $_a$(x=0.85)=-7.95, $_c$(x=0.85)=1.26, $_a$(x=0.875)=-2.87, $_a$(x=0.875)=-6.28, $_b$ (x=0.85)=10.6). This is an indication that the LT-O phase is the same both compounds and that the orbital order of the monoclinic low temperature phase in x=0.875 is less perfect.

Fig. 8-62 *Rietveld plots of the RT and low temperature SXRPD patterns of $Bi_{0.125}Ca_{0.875}MnO_3$ compound*
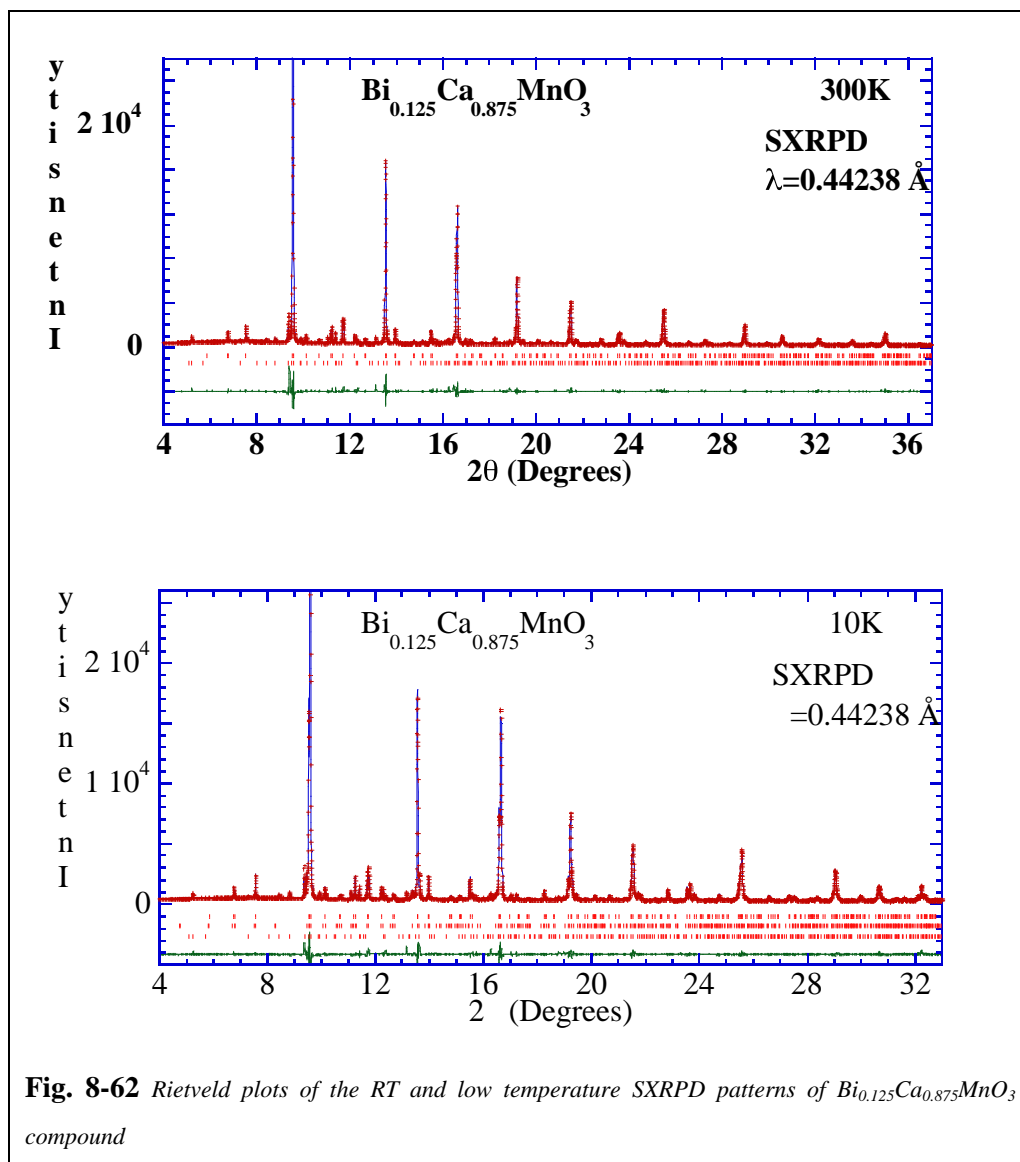
8.4.4.2 Magnetic structures of $Bi_{0.125}Ca_{0.875}MnO_3$

The analysis of the D20-NPD patterns at 10K for the x=0.875 sample revealed the existence of two magnetic phases (Fig. 8-63, Fig. 8-64). A C-type structure was found associated to the minority monoclinic phase while a G type magnetic structure was found associated to the majority orthorhombic phase as in the case of x=0.85 compound.
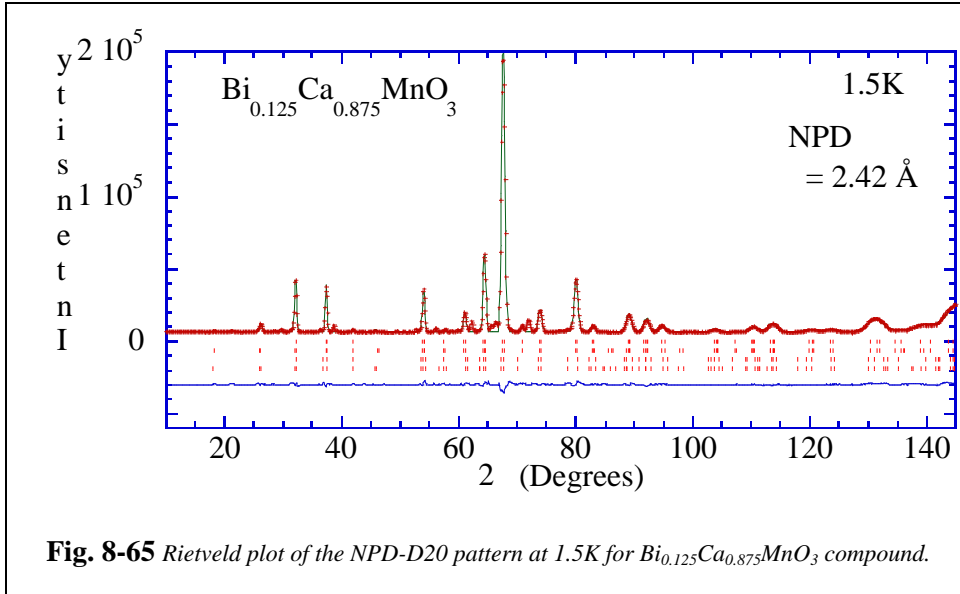
From simple inspection of the difference between the HT and LT patterns, it is evident that in this compound there exists also a long range FM component in the magnetic structure. In Fig. 8-63 are shown the low angle region of the 7K and 171K NDP patterns. In the LT pattern can be observed that in addition to the apparition of new peaks at low angles associated to AF order, there exist a relevant coherent FM contribution to the (020) orthorhombic peak as in the case of the x=0.85 sample.
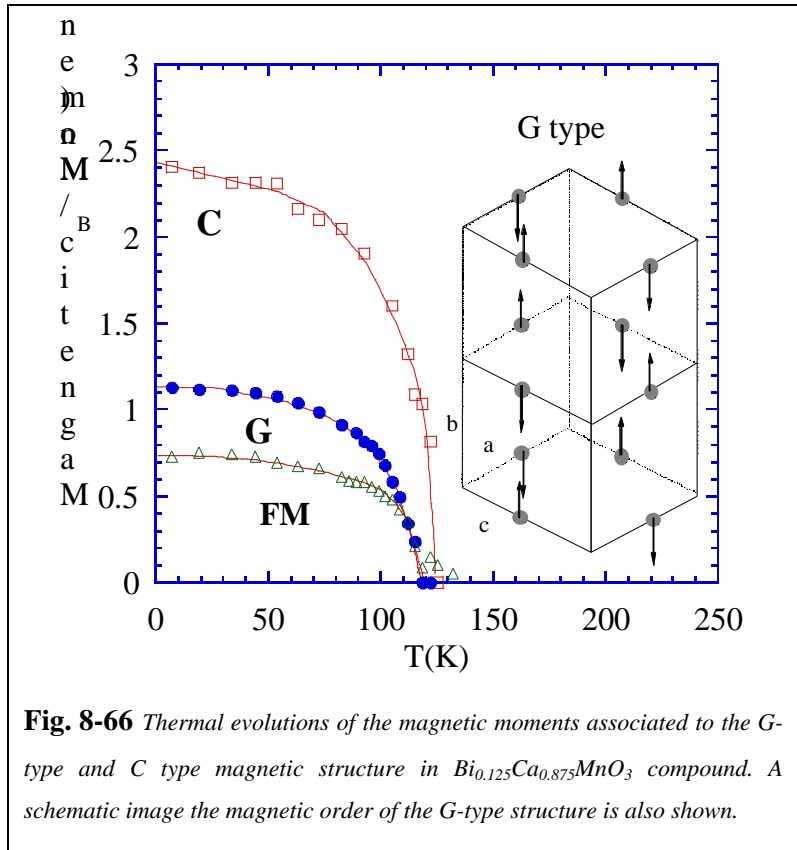

Fig. 8-63 *Difference between the 171K and 7K NPD patterns on $Bi_{0.125}Ca_{0.875}MnO_3$ compound displaying the apparition of new Bragg peaks associated to the magnetic ordering.*

Fig. 8-64 *Refined magnetic peaks of the 1.5K NPD pattern of $Bi_{0.125}Ca_{0.875}MnO_3$*
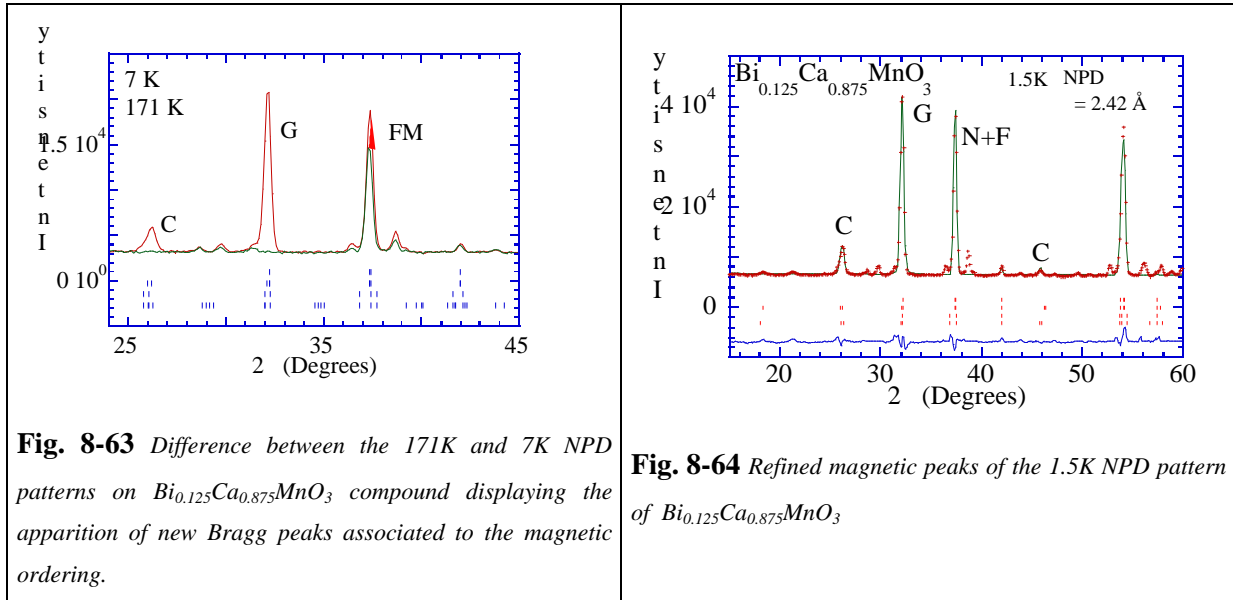
In Fig. 8-65 is shown the refinement of the whole NPD pattern with the above mentioned magnetic structures. Similarly, to the case of $Bi_{0.15}Ca_{0.85}MnO_3$, the FM contribution is simulated as a canting of the G type magnetic structure. The results of the magnetic refinement are given in Tab. 8-XVI.

Tab. 8-XVI *Refined magnetic moments and propagation vectors found in $Bi_{0.125}Ca_{0.875}MnO_3$ at 1.5K*

x	0.875	
	Pnma	P2$_1$/m
k	(0,0,1)	(_ ,0,_)
Mn	(-,G$_y$,F$_z$)	(C$_x$,-,C$_z$)
m$_x$,m$_y$,m$_z$ (μ$_B$)	0,1.13(3),0.75(2)	1.8(2),-,1.6(2)
M$_{tot}$ (μ$_B$)	1.35(4)	2.4(3)
R$_{f-mag}$	7	17

Fig. 8-65 *Rietveld plot of the NPD-D20 pattern at 1.5K for $Bi_{0.125}Ca_{0.875}MnO_3$ compound.*

From the NPD data refinements using D20 we have analysed the thermal evolution of the magnetic moment associated to each AFM structure in the x=0.875 sample. In Fig. 8-57 it is schematically shown the magnetic and orbital order found in the monoclinic C-type phase which is the minority phase in x=0.875 sample and the majority phase in the x=0.85 while in Fig. 8-66 is shown the magnetic order of the majority orthorhombic phase in x=0.875 sample and minority phase in the x=0.85 sample. The parent compound $CaMnO_3$ below T_N 122K is also characterised by this magnetic order. In $CaMnO_3$ there exist only Mn^{+4} ions and the dominant magnetic interaction is AF SE interactions between t_{2g} orbitals, thus giving the G type magnetic structure. However, in the present case the existence of defects (or electrons) is at the origin of the existence of FM domains with the same orthorhombic nuclear structure which orders at the same temperature than the G and C type magnetic domains.

Fig. 8-66 *Thermal evolutions of the magnetic moments associated to the G-type and C type magnetic structure in $Bi_{0.125}Ca_{0.875}MnO_3$ compound. A schematic image the magnetic order of the G-type structure is also shown.*

An interesting finding is that in x=0.85 and x=0.875 bismuth compounds the magnetic ordering develops at 125K which

corresponds to the transition temperature of the parent compound CaMnO$_3$. The FM ordering has also been found to develop at this temperature as shown in Fig. 8-55.

8.4.4.3 Weak ferromagnetism at low temperature in x=0.875

In x=0.875 compound weak FM has been found. The estimated FM moment is about 0.75(2)μ_B/Mn, slightly smaller than in the x=0.85 compound. However, as the orthorhombic phase is majoritary in x=0.875 compound, the FM intensity at the Bragg peaks is more easily distinguished and it makes more evident that ferromagnetism comes from the existence of long range and not from short range FM ordering.

The inspection of the thermal evolution of the magnetisation reveals larger magnetisation at 4K and low fields in the x=0.875 than in x=0.85 (Fig. 8-40, Fig. 8-41) corroborating the existence of a larger number of FM domains in the x=0.875 compound.

High magnetic field measurements performed on this sample (Fig. 8-43) reveal that at low fields the compound has a magnetisation of about 1μ_B/Mn and larger applied magnetic fields (up to 50T) are unable to saturate the sample (the spontaneous magnetisation at 4K being about 1.4μ_B/Mn).

The application of a magnetic field of 1T gives a MR of 20% at low temperature which is less than what was found in x=0.85 compound while an applied field of 7T gives a MR of about 50%. However, from the magnetic point of view the magnetisation has not changed too much. In addition the residual resistivity in x=0.875 compound is several orders of magnitude smaller than in x=0.85 compound (Fig. 8-37) and a relatively small magnetic field (1T) turns the material metallic at low temperature.

The observations described above lead us conclude that electrical percolation is the most likely phenomena governing the electrical transport of these compounds. The lower MR in x=0.875 compound can be understood considering the existence of larger FM domains already existing at zero applied magnetic field. In addition, below the magnetic transition (T 125K) the electrical resistivity of the compound do not show a sharp increase as would be expected at the AFM transition but it reduces its slope. This is an indication that the energy barrier has been reduced and we think that it is because T 125K is also the FM transition and thus as the FM interaction seems to be mediated by DE, the energy barrier for electrical conduction is reduced.

8.4.5 Conclusions

In conclusion, we have performed a detailed study on the x=0.85 and x=0.875 compounds of the heavily doped region in the phase diagram of Bi$_{1-x}$Ca$_x$MnO$_3$.

_____

Detailed analysis based on joint refinements using high resolution NPD and SXRPD revealed the existence of macroscopic phase segregation in both compounds.

The two phases have been identified and characterised in x=0.85 compound. At low temperature we found the coexistence of a orthorhombic (Pnma) phase which developed a G-type magnetic ordering and a monoclinic ($P2_1/m$) phase which developed a C-type magnetic ordering associated to a polarisation of the d_z^2 Mn orbitals in the (10-1) direction.

In addition, phase coexistence has been demonstrated to exist at all temperatures even if at RT high resolution SXRPD measurements did no permit to resolve the two phases. Phase coexistence is unmasked at the temperature where the orbital ordering develops in the phase exhibiting the C-type order at low temperatures (monoclinic phase). That means that the orbital ordering is at the origin of the orthorhombic to monoclinic phase transition of one of the phases.

A remarkable finding of this study has been to understand the origin of the phase segregation. Several possibilities were proposed to explain macroscopic phase segregation phenomena in heavily doped compounds at the moment of writing the present study. The most extended explanation was that the phase separation phenomena in highly doped compounds was produced due to intergranular strain between nucleation centres of transformed sample and non transformed sample as pointed out by [162]. Nevertheless, our data clearly shows that the low temperature non-transformed phase displays less broadening due to strain than the high temperature orthorhombic phase. Therefore, intergranular strain has been ruled out to explain the phase segregation phenomena.

Electronic phase segregation has also been ruled out as the particle sizes estimated from high resolution SXRPD for the x=0.85 compound are at least 1000Å-2000Å.

Our results reveal that the most likely origin of the phase segregation is the stabilisation of Ca vacancies in the monoclinic phase (C-type) while the orthorhombic phase (G-type) was found to be non Ca deficient.

The origin of the weak ferromagnetism in heavily doped compounds has been found to be associated to large FM domains in the G-type orthorhombic phase. In addition, the ferromagnetic order was found to develop below T_N=125K in both compounds, which also corresponds to the transition temperature in the parent compound $CaMnO_3$. Hence the origin of the FM domains seems to be an electronic phase separation in the orthorhombic low temperature G-type phase similar to the one of $Pr_{2/3}Ca_{1/3}MnO_3$ compound presented in chapter 7.

Magnetoresistance in these compounds has been explained on the basis of percolative model similarly to the model used to explain the origin of the large CMR in x=1/3 compounds [229]. The magnetic interaction in the FM domains seems to be governed by double exchange interaction. Hence, when the G-type magnetic order develops in the orthorhombic phase, it should be energetically more favourable to expulse the e_g electrons from the domains developing the G-type magnetic order and to

form domains with an excess of electrons which will develop FM order and display metallicity. However, these domains are spread out in the orthorhombic phase and thus they are badly connected giving rise to an insulating macroscopic resistivity. The application of an external magnetic field will favour the FM state and thus help to connect different FM domains, diminishing the resistivity. When continuous FM paths are constructed, the macroscopic resistivity turns to metallic even if the magnetisation if far from displaying saturation.

These explanations also permit to understand the structural, magnetic, and electric behaviour of the x=0.875 compound. This intrinsic phenomenon make us propose a major revision of the phase diagram in the heavily doped region in manganites.